

High-Fidelity, Frequency-Flexible Two-Qubit Fluxonium Gates with a Transmon Coupler

Leon Ding,^{1, 2, *} Max Hays,² Youngkyu Sung,^{2, 3, †} Bharath Kannan,^{2, 3, †} Junyoung An,^{2, 3}
 Agustin Di Paolo,^{2, ‡} Amir H. Karamlou,² Thomas M. Hazard,⁴ Kate Azar,⁴ David K. Kim,⁴
 Bethany M. Niedzielski,⁴ Alexander Melville,⁴ Mollie E. Schwartz,⁴ Jonilyn L. Yoder,⁴ Terry P. Orlando,²
 Simon Gustavsson,^{2, §} Jeffrey A. Grover,² Kyle Serniak,^{2, 4} and William D. Oliver^{1, 2, 3, 4, ¶}

¹Department of Physics, Massachusetts Institute of Technology, Cambridge, MA 02139, USA

²Research Laboratory of Electronics, Massachusetts Institute of Technology, Cambridge, MA 02139, USA

³Department of Electrical Engineering and Computer Science,
Massachusetts Institute of Technology, Cambridge, MA 02139, USA

⁴MIT Lincoln Laboratory, Lexington, MA 02421, USA

(Dated: April 14, 2023)

We propose and demonstrate an architecture for fluxonium-fluxonium two-qubit gates mediated by transmon couplers (FTF, for fluxonium-transmon-fluxonium). Relative to architectures that exclusively rely on a direct coupling between fluxonium qubits, FTF enables stronger couplings for gates using non-computational states while simultaneously suppressing the static controlled-phase entangling rate (ZZ) down to kHz levels, all without requiring strict parameter matching. Here we implement FTF with a flux-tunable transmon coupler and demonstrate a microwave-activated controlled-Z (CZ) gate whose operation frequency can be tuned over a 2 GHz range, adding frequency allocation freedom for FTF's in larger systems. Across this range, state-of-the-art CZ gate fidelities were observed over many bias points and reproduced across the two devices characterized in this work. After optimizing both the operation frequency and the gate duration, we achieved peak CZ fidelities in the 99.85–99.9% range. Finally, we implemented model-free reinforcement learning of the pulse parameters to boost the mean gate fidelity up to $99.922 \pm 0.009\%$, averaged over roughly an hour between scheduled training runs. Beyond the microwave-activated CZ gate we present here, FTF can be applied to a variety of other fluxonium gate schemes to improve gate fidelities and passively reduce unwanted ZZ interactions.

I. INTRODUCTION

Over the past two decades, superconducting qubits have emerged as a leading platform for extensible quantum computation. The engineering flexibility of superconducting circuits has spawned a variety of different qubits [1–7], with an abundance of different two-qubit gate schemes [8–16]. More recently, tunable coupling elements have aided efforts to scale to larger multi-qubit systems [17], including a demonstration of quantum advantage with 53 qubits [18] and quantum error correction improving with code distance in the surface code [19]. While there exists a large selection of superconducting qubits, almost all advancements toward processors at scale have been carried forward with the transmon qubit [4], a simple circuit consisting of a Josephson junction in parallel with a shunt capacitance. However, that simplicity comes at a cost. A relatively large transition frequency (~ 5 GHz) makes the transmon more sensitive to dielectric loss [20], and a weak anharmonicity (~ -200 MHz) presents a challenge for both performing fast gates and designing multi-qubit processors.

The fluxonium qubit [5, 21, 22] is a promising alternative to the transmon for gate-based quantum information processing [23], which alleviates both of these drawbacks. The fluxonium circuit consists of a capacitor (typically smaller than that of a transmon), a Josephson junction, and an inductor all in parallel. The transition frequency between the ground and first excited state of the fluxonium is usually between 100 MHz and 1 GHz at an external flux bias of $0.5 \Phi_0$. At these low operating frequencies, energy relaxation times T_1 exceeding 1 ms [24, 25] have been observed, alongside anharmonicities of several GHz. With these advantages, fluxonium qubits have already achieved single-qubit gate fidelities above 99.99% [25]. Two-qubit gates relying on capacitive coupling [26–30], however, are more challenging because the same small transition matrix elements which improve T_1 concomitantly reduce the interaction strength between qubits. Moreover, direct capacitive coupling results in an undesired, always-on entangling rate (ZZ). In previous works, a variety of strategies were employed to reduce the ZZ , such as keeping coupling strengths small or using ac-Stark drives, all of which have their own individual drawbacks. Finally, two-qubit gates must also reliably contend with frequency collisions with spectator qubits if they are to be scaled to larger arrays of qubits without sacrificing fidelity.

In this work, we introduce the fluxonium-transmon-fluxonium circuit (FTF) as a novel architecture for coupling fluxonium qubits via a transmon coupler [Fig. 1(a)].

* leonding@mit.edu

† Present address: Atlantic Quantum, Cambridge, MA 02139

‡ Present address: Google Research, Mountain View, CA, USA.

§ Additional address: Atlantic Quantum, Cambridge, MA 02139

¶ william.oliver@mit.edu

FTF suppresses the static ZZ down to kHz levels in a manner nearly insensitive to design parameter variations while simultaneously providing strong couplings for two-qubit gates via non-computational states. Using FTF, we propose and demonstrate a microwave-activated CZ gate between two fluxonium qubits in a 2D-planar geometry. This gate takes advantage of strong capacitive couplings which create a manifold of highly hybridized states that mix the first higher transition ($|1\rangle \leftrightarrow |2\rangle$) of both fluxonium qubits with the transmon's lowest transition ($|0\rangle \leftrightarrow |1\rangle$). Despite these strong couplings, the computational states remain relatively unhybridized due to the large qubit-coupler detuning, allowing for high-quality single-qubit gates in addition to the two-qubit gate. We applied microwave pulses to drive a full oscillation to and from this manifold contingent on both fluxonium qubits starting in their excited states and benchmarked an average CZ gate fidelity of up to $99.922 \pm 0.009\%$ in 50 ns via Clifford-interleaved randomized benchmarking.

The flux tunability of the transmon coupler also allows for the operation of the CZ gate at a wide range of microwave drive frequencies, providing a convenient way to avoid frequency collisions *in situ* in larger-scale devices. Such *in situ* tunability is critical for microwave-activated gates, as dependence on a particular frequency layout places an exponentially difficult demand on fabrication precision [31, 32] as the number of qubits increases. Our devices also exhibit up to millisecond T_1 in a multi-qubit planar geometry, placing them among the highest coherence superconducting qubits to date and priming them for use in larger systems.

II. FTF ARCHITECTURE

Our device configuration consists of two differential fluxonium qubits capacitively coupled to a grounded transmon coupler, with a much weaker direct capacitive coupling between the two fluxonium qubits [Fig. 1(b)]. The two lowest-lying states of each fluxonium form the computational basis $\{|00\rangle, |01\rangle, |10\rangle, |11\rangle\}$, and the first excited state of the coupler, in addition to the second excited states of the fluxonium qubits, serve as useful non-computational states. Modeling only the qubits and their pairwise capacitive couplings, our system Hamiltonian is

$$\begin{aligned} \hat{H}/h = & \sum_{i=1,2} 4E_{C,i}\hat{n}_i^2 + \frac{1}{2}E_{L,i}\hat{\phi}_i^2 - E_{J,i}\cos(\hat{\phi}_i - \phi_{\text{ext},i}) \\ & + 4E_{C,c}\hat{n}_c^2 - E_{J1,c}\cos(\hat{\phi}_c) - E_{J2,c}\cos(\hat{\phi}_c - \phi_{\text{ext},c}) \\ & + J_{1c}\hat{n}_1\hat{n}_c + J_{2c}\hat{n}_2\hat{n}_c + J_{12}\hat{n}_1\hat{n}_2, \end{aligned} \quad (1)$$

where E_C , E_J , and E_L represent the charging, Josephson, and inductive energies, respectively. Subscripts $i = 1, 2$ index the two fluxonium nodes, and subscript c labels the coupler node. Here we also introduced

the external phase ϕ_{ext} , which is related to the external flux Φ_{ext} through the expression $\Phi_{\text{ext}}/\Phi_0 = \phi_{\text{ext}}/2\pi$ for each qubit. For both our main device (Device A) and a secondary device (Device B), the experimentally obtained Hamiltonian parameters are listed in Table I, along with the measured coherence times.

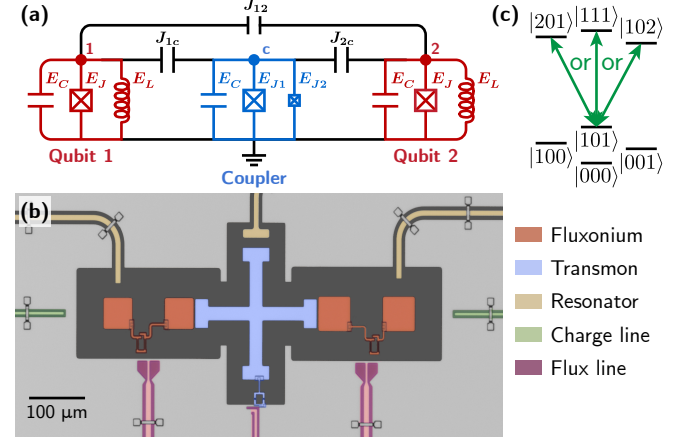


FIG. 1. Device overview and gate principle. (a) Simplified circuit schematic of two fluxonium qubits (red) capacitively coupled to a tunable-transmon coupler (blue). (b) False-colored optical micrograph of the two fluxonium qubits and the transmon along with their readout resonators, charge lines, and local flux lines. Arrays of 102 Josephson junctions in series form the fluxonium inductances. (c) Energy level diagram illustrating the principle of the CZ gate. In practice, levels $|201\rangle$, $|102\rangle$, and $|111\rangle$ are highly hybridized, and selectively driving any of these transitions results in a CZ gate.

A. Gate principles

The operating principles of FTF are fundamentally different than those of all-transmon circuits [17]. Due to its relatively high frequency, the coupler interacts negligibly with the computational states of the qubits. Instead, the coupler predominantly interacts with the higher levels of the qubits, acting as a resource for two-qubit gates without adversely affecting single-qubit gates.

We describe the quantum state of the system using the notation $|jkl\rangle$, where j , k , and l denote the energy eigenstates in the uncoupled basis of fluxonium 1, the coupler, and fluxonium 2, respectively. While coupler-based gates are often activated by baseband flux pulses, here we generate the required entangling interaction via a microwave pulse from $|101\rangle$ to a non-computational state of the joint system. As illustrated in Fig. 1(c), a single-period Rabi oscillation from $|101\rangle$ to either $|201\rangle$, $|111\rangle$, or $|102\rangle$ gives the 180° conditional phase shift necessary for a CZ gate, provided no other transitions are being driven. We note that, throughout this work, we label the eigenstates according to their maximum overlap with the uncoupled qubit/coupler states at $\Phi_{\text{ext},c} = 0$

TABLE I. Characterization of FTF devices. Hamiltonian parameters for both Device **A** and Device **B** were obtained by fitting two-tone spectroscopy data and the static ZZ rate vs. coupler flux. Coherence times were measured by biasing each fluxonium at $\Phi_{\text{ext}} = 0.5 \Phi_0$ using only the global flux bias. Unless otherwise stated, all data in this manuscript corresponds to Device A.

	E_C (GHz)	E_L (GHz)	E_J (GHz)	N_{JJ}	$\omega_{01}/2\pi$ (GHz)	$\omega_r/2\pi$ (GHz)	T_1 (μs)	T_2^R (μs)	T_2^E (μs)
A	Fluxonium 1	1.41	0.80	6.27	102	0.333	7.19	560	160
A	Fluxonium 2	1.30	0.59	5.71	102	0.242	7.08	1090	70
A	Transmon c	0.32		3.4, 13	—	—	7.30	—	—
B	Fluxonium 1	1.41	0.88	5.7	102	0.426	7.20	450	230
B	Fluxonium 2	1.33	0.60	5.4	102	0.281	7.09	1200	135
B	Transmon c	0.30		3.0, 13	—	—	7.31	—	310
J_{1c} (MHz)				J_{2c} (MHz)			J_{12} (MHz)		
A	Coupling strengths	570				560			125
B	Coupling strengths	550				550			120

(equivalently $\Phi_{\text{ext},c} = 1 \Phi_0$). We perform this labeling at $\Phi_{\text{ext},c} = 0$ because tuning the coupler flux results in avoided crossings among the higher levels of the system.

In general, stronger coupling strengths result in larger detunings from parasitic transitions in two-qubit gate schemes, yet doing so often results in unintended consequences. Two common drawbacks of larger coupling strengths are remedied using the FTF architecture: (1) crosstalk due to non-nearest-neighbor couplings, and (2) unwanted static ZZ interactions. In all transmon-based architectures, the same level repulsion that enables the two-qubit gate also creates level repulsions within the computational subspace. This is because all transition frequencies and charge matrix elements of adjacent levels in a transmon have similar values. As this hybridization among the computational states increases, charge drives will produce non-local microwave crosstalk to unwanted qubit transitions. In FTF, the large ratio of transition matrix elements $|\langle 2| \hat{n} |1\rangle| / |\langle 1| \hat{n} |0\rangle|$ for fluxonium qubits, the large fluxonium anharmonicity, and the large detunings between the transmon and each fluxonium all serve to mitigate these negative side-effects.

B. ZZ reduction

Formally, the ZZ interaction rate is defined as $\zeta = (E_{11} - E_{10} - E_{01} + E_{00})/h$ (for two qubits) or $\zeta = (E_{101} - E_{100} - E_{001} + E_{000})/h$ (for two qubits and a coupler). It describes an unwanted, constant, controlled-phase-type entangling rate caused by the collective level repulsions from the many non-computational states of superconducting qubits acting on the computational states.

A key feature of the FTF architecture is its ability to suppress ζ , despite the strong coupling strengths that would typically amplify it. This low ζ can be understood by considering the couplings J_{ij} perturbatively up to fourth order. At each order m , the perturbative correction can be considered an m th-order virtual transition between the states of the uncoupled qubits; the strength

of a particular transition is proportional to the product of the corresponding couplings J_{ij} . In Fig. 2(a), we illustrate the dominant virtual transitions up to fourth order: the first-order correction is zero; at second order, only direct transitions between the two fluxonium qubits contribute to ζ ; at third order, the only allowed transitions form three-cycles between the three qubits; and at fourth order, we find that transmon-mediated transitions between the two fluxonium qubits dominantly contribute to ζ . As such, we can write ζ to fourth order as

$$\zeta \approx J_{12}^2 \zeta^{(2)} + J_{12} J_c^2 \zeta^{(3)} + J_c^4 \zeta^{(4)}, \quad (2)$$

where $\zeta^{(i)}$ depend only on the uncoupled states, and we assume $J_{1c} = J_{2c} = J_c$. Specifically, we find our device to be well-described by $\zeta^{(2)} = -2.1 \times 10^{-3} \text{ GHz}^{-1}$, $\zeta^{(3)} = 1.4 \times 10^{-3} \text{ GHz}^{-2}$, and $\zeta^{(4)} = -2.6 \times 10^{-4} \text{ GHz}^{-3}$ at $\Phi_{\text{ext},c} = 0.5 \Phi_0$. Critically, both the second- and fourth-order terms are negative, while the third-order term is positive. This is a direct consequence of the perturbation theory: for virtual transitions to excited states above the computational subspace, even-order terms describe level repulsions, while odd-order terms describe level attractions. The relatively low ZZ in the FTF system stems from this cancellation between even and odd terms (see Appendix C for further details on the ZZ cancellation).

To understand this quantitatively, we numerically calculate ζ by diagonalizing Eq. (1) as a function of J_c and J_{12} [Fig. 2(b)]. We find that ζ can be almost perfectly canceled by appropriate choices of the couplings, as traced by the darker dashed line. Within perturbation theory, this curve of minimum ζ is a parabola: $d\zeta/dJ_{12} = 0 \rightarrow J_{12} = -J_c^2 \zeta^{(3)}/2\zeta^{(2)}$. By inserting this expression into Eq. (2), we obtain the dependence of ζ along the parabola $\zeta_{\min} = J_c^4 (-\zeta^{(3)} \zeta^{(3)}/4\zeta^{(2)} + \zeta^{(4)})$. For our device parameters, the two terms in parentheses almost cancel, summing to $-2 \times 10^{-6} \text{ GHz}^{-3}$.

Importantly, $|\zeta|$ remains below 10 kHz for J_c values of up to 1 GHz, while maintaining the optimal coupling ratio. To take full advantage of this phenomenon, we

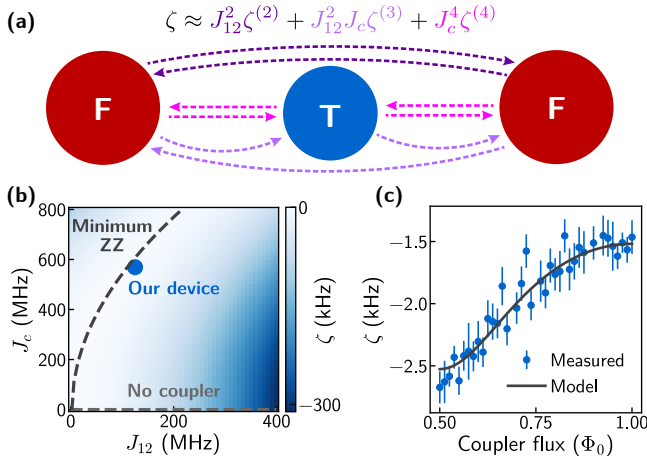


FIG. 2. ZZ-reduction in the FTF architecture. (a) A perturbative treatment of the couplings J_{ij} shows energy shifts in FTF to be dominated by virtual transitions (dashed arrows) of second (dark purple), third (light purple), and fourth (pink) order between the fluxonium qubits (maroon circles) and the coupler (blue circle). (b) Numerical simulation of ζ as a function of $J_c = J_{1c} = J_{2c}$ and J_{12} with the experimentally extracted qubit parameters. With the coupler, a ratio of coupling strengths always exists that minimizes ζ (dark gray). (c) Measured and simulated ζ as a function of the coupler flux for the experimental device parameters. The ZZ rate remains nearly constant between -1.5 and -2.7 kHz.

designed the coupling strengths to be as large as reasonable for our geometry. Furthermore, by choosing the transmon to have a grounded geometry, a near-optimal ratio of J_c^2/J_{12} is maintained while freely varying the fluxonium-transmon capacitance (see Appendix B for full details). In addition to this insensitivity to the underlying coupling capacitance, ζ is only weakly dependent on J_c , and J_{12} : independent errors in J_c and J_{12} by up to 20% would increase ζ in our device by a maximum of 11 kHz (modeling the worst case scenario in which J_{12} increases and J_c decreases). Such robustness will be critical in larger-scale devices, as capacitive coupling strengths cannot be changed after device fabrication and are subject to fabrication variations.

The value of ζ is also insensitive to the coupler frequency, allowing us to safely bias the system at any $\Phi_{\text{ext},c}$. This is unsurprising, as the coupler energy levels are far from any resonances with the computational states. In other words, any change in the coupler frequency must compete with the large detuning between the coupler and fluxonium $|0\rangle \leftrightarrow |1\rangle$ transitions. To validate our models, we experimentally determined ζ by measuring the frequency of fluxonium 1 using a Ramsey experiment while preparing fluxonium 2 in the ground or excited state. Taking the difference in fitted frequencies associated with the two initial state preparations yields the experimental value of ζ , which we find to closely follow our numerical simulations as a function of the coupler flux [see Fig. 2(c)]. An alternative approach to ZZ

reduction with fluxonium qubits is to apply always-on ac-Stark drives [27, 30]. While this is an effective means to reduce ZZ in few-qubit devices, the requirement of an additional calibrated drive per qubit becomes increasingly prohibitive as system sizes grow.

III. GATE CALIBRATION

Before discussing our single- and two-qubit gates, we first describe the qubit readout and flux biasing. In thermal equilibrium, our fluxonium qubits have nearly equal populations in the ground and excited states ($k_B T > \hbar\omega_{01}$). To address this, we initialized each qubit in either the ground or excited state at the beginning of each experiment via projective readout and heralded the desired initial state [33] (see Appendix D for further details). To realize independent qubit initialization in our system, each qubit was capacitively coupled to a separate readout resonator, allowing us to perform high-fidelity, single-shot readout within the full computational basis. All three resonators were further coupled to a common Purcell filter [34].

We used a global biasing coil to tune the flux across the entire device and used additional local flux lines biased through coaxial cables for independent control of each qubit. This allowed us to freely change the coupler flux while holding each fluxonium at $\Phi_{\text{ext}} = 0.5\Phi_0$. Although only DC flux was required in our experiment, our device is fully compatible with fast-flux pulses. As such, FTF presents an opportunity to investigate iSWAP, Landau-Zener, or other flux-modulated gates in a system with low static ZZ rates [14, 15, 26, 35–37].

Unfortunately, we found that our qubit coherence times were sensitive to bias-induced heating from the coaxial flux lines. We have found that both qubit T_1 and T_2 (both Ramsey and spin-echo) drop with increasing current. To minimize this effect when performing two-qubit experiments, the global coil was used to simultaneously bias the two fluxonium qubits as close as possible to their operation points $\Phi_{\text{ext},1} = \Phi_{\text{ext},2} = 0.5\Phi_0$. The local flux lines were then used to more precisely tune $\Phi_{\text{ext},1}$ and $\Phi_{\text{ext},2}$ and bias the coupler flux. We emphasize that this nonideality is not fundamental nor unique to the FTF architecture and can be improved in future experiments by optimized construction and filtering of our flux-bias lines.

A. Single-qubit gates

To deconvolve the aforementioned heating effects from the measurement results, we biased the qubits solely with the global coil when characterizing individual qubit coherences (see Table I). Notably, fluxonium 2 in our device achieves a lifetime of over a millisecond, with similar performance reproduced in Device B (see Appendix L). In accordance with the higher qubit frequency, fluxo-

onium 1 has a shorter lifetime, and the T_2^E of all characterized qubits peaks between 200-300 μ s, likely limited by photon-shot noise from occupation of the resonator or filtering of the flux lines.

We realized single-qubit gates by calibrating Rabi oscillations generated by a resonant charge drive using a cosine pulse envelope. To quantify the fidelities of these gates, we performed individual as well as simultaneous Clifford randomized benchmarking (RB) using a microwave-only gate set, $\{I, \pm X, \pm Y, \pm X_{\pi/2}, \pm Y_{\pi/2}\}$, to generate the Clifford group, resulting in an average of 1.875 gates per Clifford [12, 38]. In our decomposition, all gates had an equal time duration and were derived from a single calibrated X_π pulse by halving the amplitude and/or shifting its phase (see Appendix E for the full calibration sequence). Here, both qubits were biased at $\Phi_{\text{ext}} = 0.5 \Phi_0$, with minimal current through the coupler flux line. In Fig. 3(a), we varied the pulse width from 10 ns to 42 ns and found average single-qubit gate fidelities consistently near or above 99.99% and show the explicit randomized benchmarking traces in Figs. 3(b-c) for a gate duration of 18 ns. In this range, the incoherent error begins to trade off with the coherent error (from violating the rotating wave approximation), with qubit 1 able to tolerate faster gates than qubit 2 due to its higher frequency. We note gates were additionally calibrated at 6 ns with significantly lower fidelities on both qubits due to large coherent errors. Overall, our fidelities from simultaneously applied gates are $< 5 \times 10^{-5}$ lower than the individually applied ones, a testament to the low ZZ rate measured in our system. We suspect the small difference in fidelity is caused by microwave crosstalk between charge lines and qubits.

B. Two-qubit CZ gate

We began our investigation of the two-qubit CZ gate by performing spectroscopy of the relevant non-computational state transitions. With the system initialized in $|101\rangle$, we swept the coupler flux $\Phi_{\text{ext,c}}$ to map out the transition frequencies to the three dressed states $|201\rangle$, $|111\rangle$, and $|102\rangle$ [see Fig. 4(a)]. Importantly, we found that $|111\rangle$ crosses both $|201\rangle$ and $|102\rangle$ (at $\Phi_{\text{ext,c}} \approx 0.65 \Phi_0$), with an avoided crossing strength of nearly 1 GHz. With such strong hybridization, a high-performance gate could be realized by driving any of the three energy levels over a wide coupler flux range. Nevertheless, the transitions yielded varying performance depending on their coherence times and the proximity of undesired transitions, whose frequencies we extracted in the same measurement by heralding different initial states (see Appendix F).

We activated the gate interaction associated with each transition by simultaneously applying a charge drive to each fluxonium [Fig. 4(b) inset]. These drives were chosen to have equal amplitude, with a relative phase between them to maximize constructive interference at the

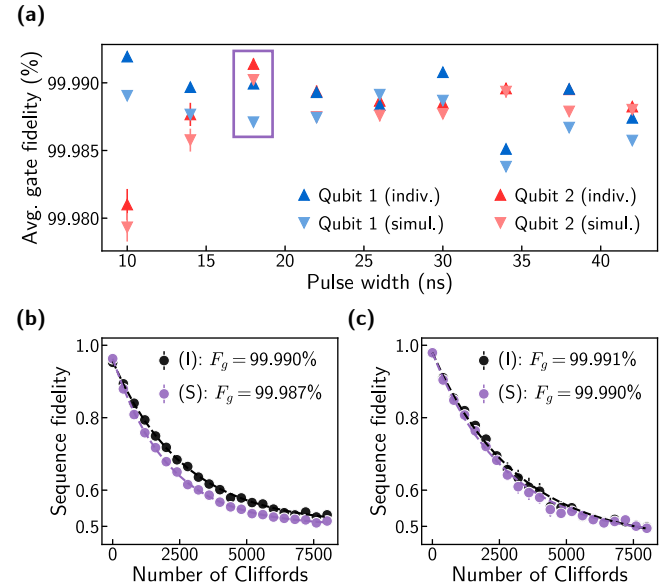


FIG. 3. **Single-qubit benchmarking on our multi-qubit device.** (a) Average single-qubit gate fidelities obtained by individual and simultaneous Clifford randomized benchmarking as a function of the pulse width. Error bars for the majority of data points are within the size of the marker and correspond to standard errors about the mean. (b-c) Individual (I) and simultaneous (S) RB traces of an 18 ns gate (purple box in (a)) for qubit 1 and qubit 2, respectively. Individual and simultaneous average gate fidelities have a standard error of about 3×10^{-6} for qubit 1 and 4×10^{-6} for qubit 2. The larger uncertainties in the qubit 2 data arise from coherent errors, which begin to dominate for gates shorter than 18 ns (red points in (a)).

intended transition. We found that using two constructive drives was a convenient method for reducing the total applied power for a given Rabi rate, resulting in a reduced ac-Stark shift from off-resonant transitions. In severe cases, a large ac-Stark shift could prevent the realization of a 180° conditional phase and increase leakage into non-computational states. An alternative approach exists to tune the relative phase and amplitude of the two drives to result in complete destructive interference of the nearest leakage transition (see Appendix G). While theoretically we expect the relative phase and amplitude to be important for reducing leakage, we found that as long as a 180° conditional phase was attainable, the CZ gate fidelity was relatively insensitive to these two parameters. Figure 4(b) shows the familiar Rabi chevrons when the transition was driven as a function of frequency; in experimental practice, our two-qubit gate is quite similar to driving single-qubit Rabi oscillations.

For a given transition and pulse duration, there are four critical parameters associated with the CZ gate to calibrate: (1) the overall drive amplitude of the two phase-locked drives to ensure a single-period oscillation, (2) the drive frequency to ensure a 180° conditional phase accumulation, and (3-4) the single-qubit phases

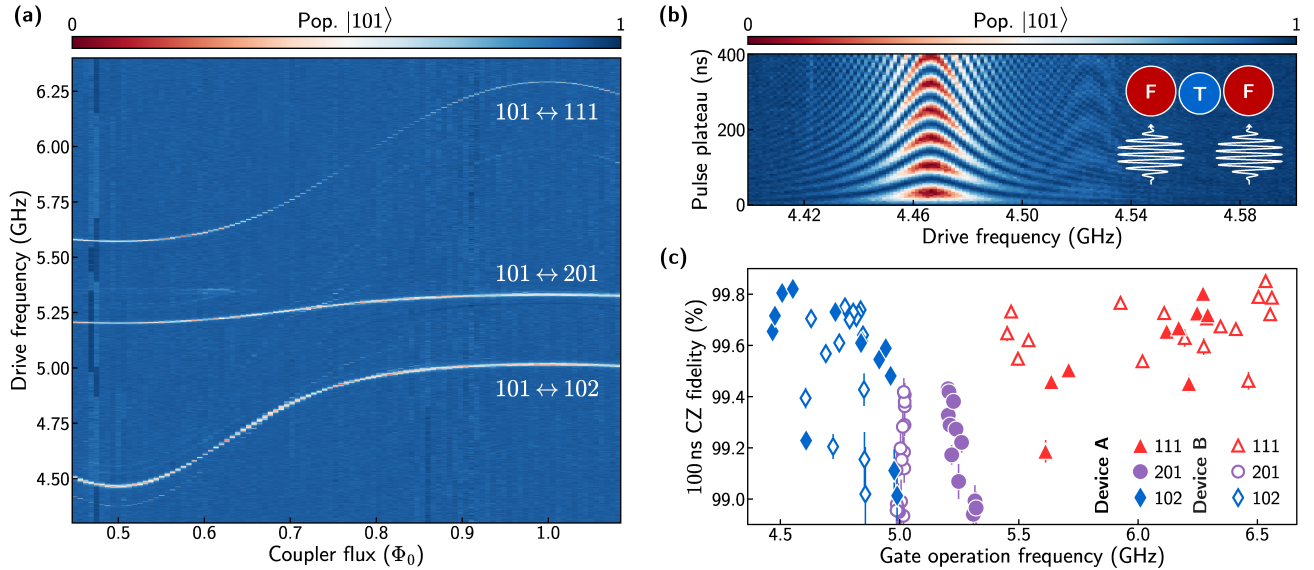


FIG. 4. CZ gate as a function of flux. (a) Spectroscopy of relevant non-computational states. The qubits were initialized in the $|101\rangle$ state via single-shot readout. (b) Time-domain Rabi oscillations of the $|101\rangle \leftrightarrow |102\rangle$ transition as a function of the drive frequency. The faint chevron pattern at 4.52 GHz arises from the $|001\rangle \leftrightarrow |002\rangle$ transition and was visible due to imperfect state initialization. In all plots, populations have been normalized to between 0 and 1. Inset shows that gates were driven with simultaneous phase-locked pulses applied to each fluxonium charge line. (c) CZ gate fidelities using a fixed 100 ns cosine pulse envelope, driving each transition in (a) across the entire $0.5 - 1\Phi_0$ range, linearly sampled over 21 points. A secondary device (Device B) with slightly different Hamiltonian parameters supports the reliability of our architecture. Points with fidelity below 98.9% correspond to failures in the automated calibration and are therefore excluded from the plot. All gate fidelities were obtained from interleaved randomized benchmarking averaged over different 20 randomizations, with error bars corresponding to the standard error.

accumulated on each fluxonium during the gate. These single-qubit phase corrections can be conveniently implemented through virtual-Z gates by adjusting the phases of subsequent single-qubit gates [39]. After calibration, we extract the gate fidelity by performing Clifford interleaved randomized benchmarking, averaging over 20 different randomizations [12, 40, 41]. Similar to our single-qubit Clifford decomposition, we generated the two-qubit Clifford group with the gate set $\{I, \pm X, \pm Y, \pm X_{\pi/2}, \pm Y_{\pi/2}, \text{CZ}\}$, yielding an average of 8.25 single-qubit gates and 1.5 CZ gates per Clifford. A more detailed gate calibration and characterization description can be found in Appendix H.

The FTF approach offers a potential solution to frequency-crowding by allowing for an adjustable gate operation frequency. To demonstrate this frequency-flexibility in our device, we linearly sampled the coupler flux $\Phi_{\text{ext},c}$ at 21 values between $0.5\Phi_0$ and $1\Phi_0$ and calibrated a CZ gate across all three transitions in Fig. 4(a) while maintaining a constant 100 ns pulse length [Fig. 4(c)]. Each data point in Fig. 4(c) represents a fully automated re-calibration of all single- and two-qubit gate parameters without manual fine-tuning. Missing points indicate either failed calibrations or fidelities lower than 98.9%, which may be caused by TLS or nearly resonant unwanted transitions (see Appendix J for further details). While these fidelities remain unoptimized over

the pulse width, they indicate the ease and robustness of the tuneup, as well as the accessibility of state-of-the-art gate fidelities at a variety of drive frequencies. We further emphasize this by including fidelities from Device B, a second fully characterized device with similar performance. While designed to be nominally identical, the non-computational states in Device B differ by up to 300 MHz from Device A, with no significant detriment to the gate fidelities (see Appendix L for additional characterization of Device B).

To investigate the trade-off between coherent and incoherent error, we characterized the gate fidelity as a function of the pulse width. In general, all fidelities in Fig. 4(c) may be improved by optimizing over this pulse width, with our highest fidelity gates using the $|101\rangle \leftrightarrow |102\rangle$ transition at $\Phi_{\text{ext},c} = 0.575\Phi_0$ [Fig. 5(a)]. At the observed optimal gate time of 85 ns for this transition, we benchmarked a CZ fidelity of $99.89\% \pm 0.02\%$. For longer gate durations, the gate error is dominated by the lifetime of the driven non-computational state, measured to be around 10 μs at this transition and, in general, varied from 5 – 20 μs across all transitions in Fig. 4(a). The coherence times of the computational states also reduce the fidelity, but for our devices this error is negligible compared to the T_1 of the non-computational state (see Appendix K for an analytic error model of this gate process). At shorter gate

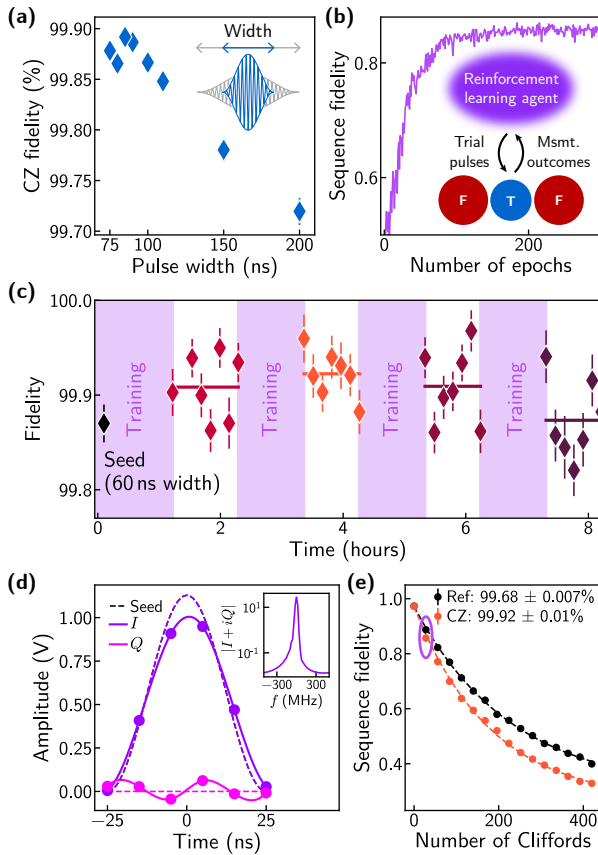


FIG. 5. Optimizing the CZ gate fidelity via reinforcement learning. (a) Gate fidelities as a function of the width of the cosine pulse envelope, averaged over 20 randomizations. The $|101\rangle \leftrightarrow |102\rangle$ transition at $\Phi_{\text{ext},c} \approx 0.575\Phi_0$ was used for these gates. (b) Fidelity of an interleaved randomized benchmarking sequence with 28 Cliffords using trial CZ gates sampled from the policy of a model-free reinforcement learning agent. After each epoch, the measurement results were used to update the agent's policy according to the PPO algorithm. (c) In a full training run, the agent was first seeded with a 50 ns cosine pulse, with an amplitude determined by a physics-calibrated 60 ns gate (black diamond) but scaled by 60/50. Then, the agent was trained to optimize the sequence fidelity of the 50 ns pulse (b). The learned gate was then repeatedly evaluated using interleaved randomized benchmarking averaged over 10 randomizations. The next round of training was seeded with the optimized pulse from the previous round. Horizontal bars indicate the averaged fidelity after each round of training. (d) Optimized pulse shape as learned by the agent. The agent was given control over six evenly-spaced $I(t)$ and $Q(t)$ voltage points (colored circles), with the pulse in between points determined by a cubic interpolation. Inset shows the Fourier transform of $I(t) + iQ(t)$. (e) Reference and interleaved randomized benchmarking curves averaged over all 70 randomizations after the second round of training (orange points in (c)). The purple circle at 28 Cliffords indicates the sequence length used for learning. All uncertainties in this figure correspond to the standard error of the mean.

lengths, coherent leakage into non-computational levels dominates the error, but due to the extreme degree of hybridization of the non-computational states and their subpar readout, we were not able to experimentally measure the location of the leaked population.

To further improve the gate fidelity, we deployed a model-free reinforcement learning agent [42–45], closely following the protocol described by Sivak *et al.* [46]. While reinforcement learning could not mitigate the incoherent errors dominating the gate at longer pulse widths, at shorter gate times (<70 ns) we found that it did offer an improvement via fine adjustments of the pulse parameters. To train the agent, we first seeded it with a physics-based pulse calibration with a pulse width of 60 ns; our physics-based calibration failed at gate times less than this. Then, with a fixed CZ pulse width of 50 ns, the agent was trained to maximize the sequence fidelity of interleaved randomized benchmarking at 28 Cliffords with a fixed random seed by optimizing the pulse shape and virtual-Z gates [Fig. 5(b)]. After each round of training, the optimized pulse was repeatedly evaluated by performing interleaved randomized benchmarking over 70 total Clifford sequences [Fig. 5(c)]. Training was then repeated using the optimized pulse shape from the previous training round as the seed for the next. For the training run shown in Fig. 5(c), the fidelity peaked after the second round of training (orange points), with a time-averaged value of $99.922 \pm 0.009\%$. A Wilcoxon signed-rank test gives 97% confidence that this mean is above 99.90%. As the run progressed, the average fidelity was observed to degrade. We hypothesize that this was due to system drifts beyond what the agent was able to mitigate.

In the data shown in Figs. 5(b-e), the agent was given full control of the I and Q quadratures of the pulse envelope as well as the single-qubit virtual-Z rotation angles. $I(t)$ and $Q(t)$ were discretized into six points equally spaced in time [Fig. 5(d)] with a cubic interpolation determining the remaining points. Perhaps the most distinctive feature of the learned pulse is the shape of $Q(t)$: while the agent was seeded with $Q(t) = 0$, the learned pulse shape displays a distinct oscillation in $Q(t)$. Although we do not fully understand the origin of this oscillation, some intuition may be gained by examining the Fourier transform of the pulse shape [Fig. 5(d) inset]. In the frequency domain, the oscillation in $Q(t)$ results in a distinct asymmetry of the pulse shape: at positive detunings from the carrier frequency, the spectral weight is suppressed, and vice versa for negative detunings. We hypothesize that this learned pulse asymmetry mitigates the effects of the nearest undesired transition, which is detuned by $\sim+65$ MHz at this bias point. However, we also note that attempts to mitigate the effects of this undesired transition using more established pulse shaping techniques did not improve the gate fidelity [47].

IV. OUTLOOK

Our work demonstrates an architecture in which high-fidelity, robustness against parameter variations, and extensibility are simultaneously realized. We observed millisecond fluxonium lifetimes despite couplings to neighboring qubits, resonators, flux lines, and charge lines, all within a 2D-planar architecture. Both the single- and two-qubit gates performed here are also simple – operating on the basis of a Rabi oscillation. The relative simplicity of this two-qubit gate was afforded by the FTF Hamiltonian and yielded a high fidelity operation across a large frequency-tunable range, reproduced across multiple devices.

One of the most notable features of the FTF scheme is the capacity for large coupling strengths while simultaneously reducing the ZZ interaction strength to kHz levels. This is all done without strict parameter matching or additional drives. In fact, even computational state gates such as iSWAP or cross-resonance can benefit from FTF by utilizing this ZZ reduction without worrying about additional complications for single- and two-qubit gates. A fixed-frequency transmon (or simply a resonator) would suffice for this use case (see Appendix C).

Despite already high gate fidelities, many avenues exist for improvement. First and foremost, the device heating when DC biasing qubits to their simultaneous sweet spot and tuning the coupler flux reduces the coherence times of our qubits. By optimizing the mutual inductance between the flux lines and the qubits and improving the thermalization and filtering of the flux lines, we anticipate improvements in future experiments. Even in the absence of local heating, we estimate a photon-shot-noise limit of $T_2 \sim 400 \mu\text{s}$, assuming an effective resonator temperature of $T_{\text{eff}} = 55 \text{ mK}$ [48]. Simply decreasing χ and κ should increase this T_2 limit at the expense of readout speed, which could be a worthwhile exchange in the high T_1 , low T_2 limit.

As is typical of fluxonium gates involving the non-computational states, the largest contribution to gate infidelity was the coherence of the $|201\rangle$, $|111\rangle$, $|102\rangle$ manifold. Yet, the lifetimes of these states were much lower than expected, given coherence times measured on transmons with similar frequencies. By optimizing regions of high electric field density that exist in our current design (notably the small fluxonium-transmon capacitor gap), we expect to improve these coherence times as well.

While fluxonium has long exhibited impressive individual qubit performance, our work demonstrates a viable path forward for fluxonium-based large-scale processors capable of pushing the boundaries of noisy intermediate-scale quantum computing.

ACKNOWLEDGMENTS

L.D. is grateful to Devin Underwood for his continued support throughout this project, especially during the lockdown years. M.H. acknowledges useful discussions with Vlad Sivak. This research was funded in part by the U.S. Army Research Office Grant W911NF-18-1-0411, and by the Under Secretary of Defense for Research and Engineering under Air Force Contract No. FA8702-15-D-0001. L.D. gratefully acknowledges support from the IBM PhD Fellowship, Y.S., and J.A. gratefully acknowledge support from the Korea Foundation for Advances Studies, and B.K. gratefully acknowledges support from the National Defense Science and Engineering Graduate Fellowship program. M.H. was supported by an appointment to the Intelligence Community Postdoctoral Research Fellowship Program at the Massachusetts Institute of Technology administered by Oak Ridge Institute for Science and Education (ORISE) through an interagency agreement between the U.S. Department of Energy and the Office of the Director of National Intelligence (ODNI). Any opinions, findings, conclusions or recommendations expressed in this material are those of the author(s) and do not necessarily reflect the views of the Under Secretary of Defense for Research and Engineering or the US Government.

L.D., M.H., and Y.S. performed the experiments and analyzed the data. L.D., M.H., and J.A. developed the theory and numerical simulations. L.D., Y.S., A.D.P., and K.S. designed the device. K.A., D.K.K., B.M.N., A.M., M.E.S., and J.L.Y. fabricated and packaged the devices. L.D., M.H., Y.S., B.K., J.A., A.H.K., and S.G. contributed to the experimental setup. T.H., T.P.O., S.G., J.A.G., K.S., and W.D.O supervised the project. L.D. and M.H. wrote the manuscript with feedback from all authors. All authors contributed to the discussion of the results and the manuscript.

Appendix A: Wiring

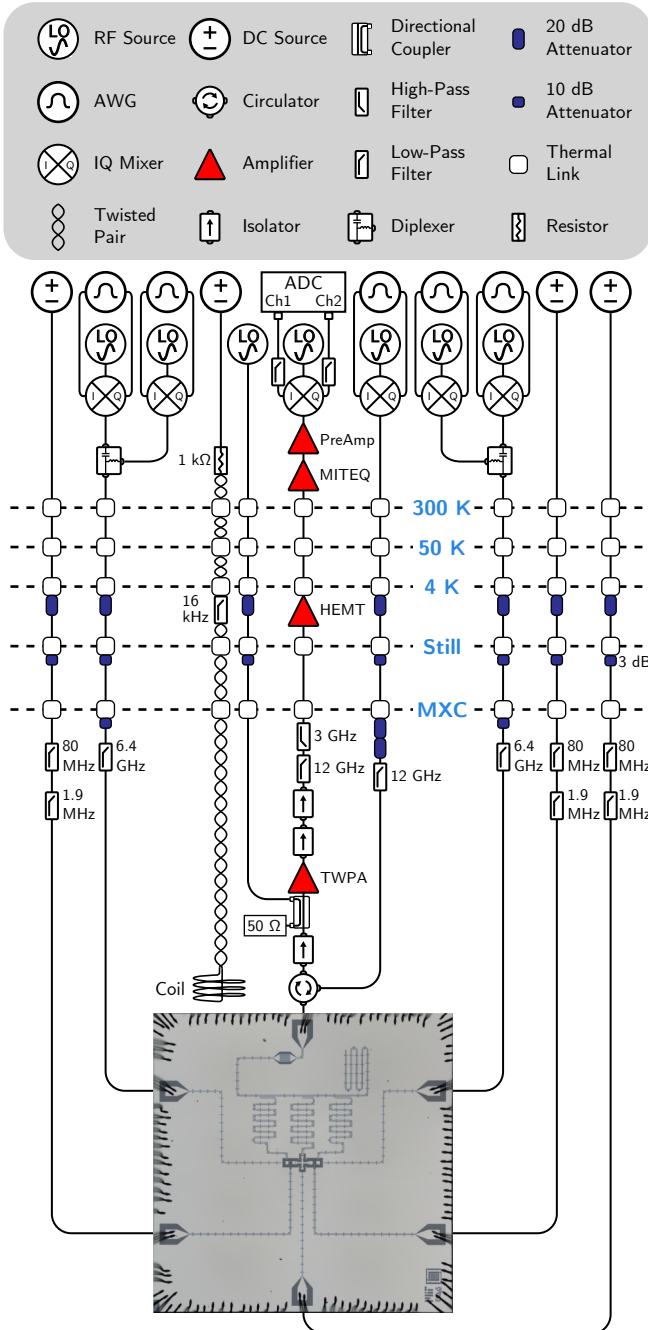


FIG. 6. A detailed wiring schematic of the experimental setup.

This experiment was conducted in a Bluefors XLD600 dilution refrigerator operated at around 20 mK, with the full wiring setup shown in Fig. 6. At the mixing chamber (MXC), the device was magnetically shielded with a superconducting can, surrounded by a Cryoperm-10 can. To reduce thermal noise from higher temperature stages, we typically used in total 23 dB attenuation for

the coupler flux lines, 30 dB attenuation for the fluxonium flux lines, 40 dB total attenuation on charge lines, and 70 dB total attenuation on the readout input – the exact value of the attenuation at Still varied between 3 dB and 10 dB across the flux lines of both devices, though this difference was not critical for any experiment. The readout output was first amplified by a Josephson traveling-wave parametric amplifier (JTWPA), pumped by a Holzworth RF synthesizer, then amplified further with a high-electron-mobility transistor (HEMT) amplifier at the 4 K stage, another HEMT at room temperature, and a final Stanford Research SR445A amplifier, before being digitized by a Keysight M3102A digitizer.

All AC signals – readout, single- and two-qubit gate pulses – were generated by single sideband mixing of Keysight M3202A 1GSa/s arbitrary waveform generators with Rohde and Schwarz SGS100A SGMA RF sources. For each qubit, the single- and two-qubit gate pulses were combined at room temperature via a diplexer from Marki Microwave (DPXN-2 for Qubit 1 and DPXN-0R5 for Qubit 2). For these dippers, the single-qubit gate frequencies occur at low enough frequencies to fall in the pass band of the DC port. All control electronics were synchronized through a common SRS 10 MHz rubidium clock.

The DC voltage bias for each qubit flux line as well as the global bobbin was supplied by a QDevil QDAC. The flux lines by design support RF flux, but in this experiment were filtered by 80 MHz and 1.9 MHz low-pass filters at the MXC. The current for the global coil was carried through a twisted pair, with a homemade 16 kHz cutoff RC filter at the 4 K stage.

TABLE II. Summary of control equipment. The manufacturers and model numbers of the control equipment used for this experiment.

Component	Manufacturer	Model
Dilution Fridge	Bluefors	XLD600
RF Source	Rohde and Schwarz	SGS100A
DC Source	QDevil	QDAC I
Control Chassis	Keysight	M9019A
AWG	Keysight	M3202A
ADC	Keysight	M3102A

Appendix B: Grounded or differential qubits?

In our circuit design, we made a conscious decision on whether each qubit (or coupler) should be made a grounded qubit or a differential qubit. By using a differential fluxonium, we reduce the amount of capacitance that coupling appendages contribute to the total effective qubit capacitance. A differential qubit also allows for a larger total area of capacitor pads for the same qubit charging energy E_C . This is important to allow for enough physical room to couple other circuit elements such as resonators, charge lines, flux lines, and other

qubits to each fluxonium.

1. Grounded transmon

The choice to use a grounded transmon, on the other hand, stems from the relationship between $J_c = J_{1c} = J_{2c}$ and J_{12} . As mentioned in the main text, to minimize the ZZ interaction ζ , we need $J_c^2/J_{12} = -2\zeta^{(2)}/\zeta^{(3)} \approx 2.97$ GHz for our device parameters. We claim that by using a grounded transmon, we can target this value of J_c/J_{12} with first-order insensitivity to the coupling capacitance (between the transmon and the adjacent fluxonium pad) C_c . Consequently, C_c becomes a free parameter in the device design, and uncertainty in its value will, to first order, have no effect on ζ . To understand this theoretically, we assume the simplified circuit schematic represented in Fig. 7(a). All capacitances not explicitly labeled are small and qualitatively unimportant in this analysis.

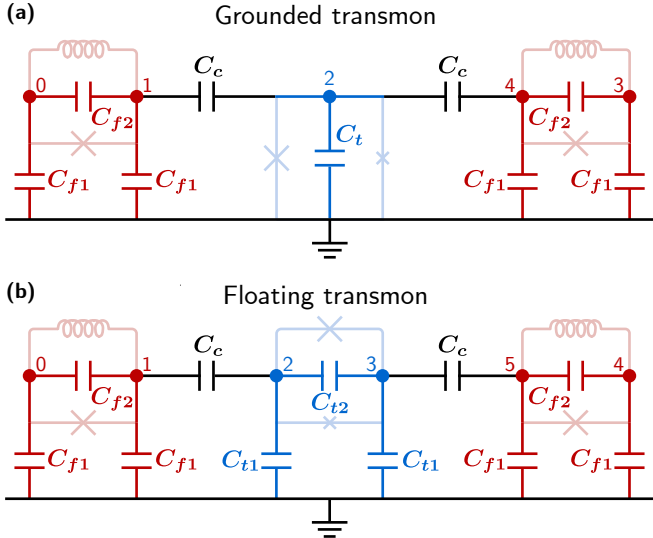


FIG. 7. Simplified circuit model of FTF circuits. (a) FTF circuit with a grounded transmon. The capacitance network is simplified for the purpose of a theoretical analysis, with no direct fluxonium-fluxonium capacitance. (b) Same circuit except with a differential transmon coupler.

We can write down the capacitance matrix of this circuit as

$$\mathbf{C} = \begin{pmatrix} C_F & -C_{f2} & 0 & 0 & 0 \\ -C_{f2} & C_F + C_c & -C_c & 0 & 0 \\ 0 & -C_c & C_t + 2C_c & 0 & -C_c \\ 0 & 0 & 0 & C_F & -C_{f2} \\ 0 & 0 & -C_c & -C_{f2} & C_F + C_c \end{pmatrix}, \quad (\text{B1})$$

where we defined $C_F = C_{f1} + C_{f2}$ for convenience. In order to isolate the relevant mode of each differential qubit, we perform a standard variable transformation into sum and difference coordinates which modifies the

capacitance matrix as $\tilde{\mathbf{C}} = (\mathbf{M}^T)^{-1} \mathbf{C} \mathbf{M}^{-1}$ with

$$\mathbf{M} = \begin{pmatrix} 1 & 1 & 0 & 0 & 0 \\ 1 & -1 & 0 & 0 & 0 \\ 0 & 0 & 1 & 0 & 0 \\ 0 & 0 & 0 & 1 & 1 \\ 0 & 0 & 0 & 1 & -1 \end{pmatrix}. \quad (\text{B2})$$

The qubit modes for each differential qubit are then solely determined by the difference coordinates, with the resultant three qubit nodes on indices 1, 2, and 4 (counting from 0). We can straightforwardly discard the modes corresponding to summed coordinates in the Hamiltonian and compute coupling strengths between nodes as $J_{ij} = 4e^2 \tilde{\mathbf{C}}^{-1}[i, j]$. Thus,

$$J_c^2/J_{12} = 4e^2 \frac{\tilde{\mathbf{C}}^{-1}[1, 2]^2}{\tilde{\mathbf{C}}^{-1}[1, 4]} \quad (\text{B3})$$

$$\approx 4e^2 \frac{1}{C_t} + \mathcal{O}(C_t^{-2}), \quad (\text{B4})$$

where we performed a Taylor expansion assuming C_c, C_{f1} , and C_{f2} are small compared to C_t in the final step. We see that to leading order, the value of J_c^2/J_{12} is solely determined by C_t^{-1} , with any dependence on C_c scaling with $\mathcal{O}(C_t^{-2})$. By inserting the designed values of $C_t = 45$ fF, $C_{f1} = 11$ fF, and $C_{f2} = 2.8$ fF, Eq. (B3) gives 2.8 GHz and Eq. (B4) gives 3.4 GHz. We emphasize that Eq. (B4) illustrates a concept in our architecture and that exact design simulations of our coupling strengths were performed using full 5×5 capacitance matrices with no mathematical approximations.

2. Differential transmon

To investigate how these relationships would compare when substituting for a differential transmon, we model the hypothetical circuit with the capacitance network in Fig. 7(b). The capacitance matrix, in this case, is

$$\mathbf{C} =$$

$$\begin{pmatrix} C_F & -C_{f2} & 0 & 0 & 0 & 0 \\ -C_{f2} & C_F + C_c & -C_c & 0 & 0 & 0 \\ 0 & -C_c & C_T + C_c & -C_{t2} & 0 & 0 \\ 0 & 0 & -C_{t2} & C_T + C_c & 0 & -C_c \\ 0 & 0 & 0 & 0 & C_F & -C_{f2} \\ 0 & 0 & 0 & -C_c & -C_{f2} & C_F + C_c \end{pmatrix} \quad (\text{B5})$$

where we have likewise defined $C_T = C_{t1} + C_{t2}$. The transformation matrix in this case is

$$\mathbf{M} = \begin{pmatrix} 1 & 1 & 0 & 0 & 0 & 0 \\ 1 & -1 & 0 & 0 & 0 & 0 \\ 0 & 0 & 1 & 1 & 0 & 0 \\ 0 & 0 & 1 & -1 & 0 & 0 \\ 0 & 0 & 0 & 0 & 1 & 1 \\ 0 & 0 & 0 & 0 & 1 & -1 \end{pmatrix} \quad (\text{B6})$$

and our coupling ratio is

$$J_c^2/J_{12} = 4e^2 \frac{\tilde{\mathbf{C}}^{-1}[1, 3]^2}{\tilde{\mathbf{C}}^{-1}[1, 5]} \quad (\text{B7})$$

$$\approx 4e^2 \frac{1}{C_{t2}} + \mathcal{O}(C_{t1}^{-1}). \quad (\text{B8})$$

While still independent of C_c to leading order, the value of $4e^2/C_{t2}$ is far too large compared to optimal values. Furthermore, FTF benefits from as high of coupling strengths as possible, and a differential transmon reduces the values of J_c and J_{12} for a fixed value of C_c .

Appendix C: ZZ cancellation in FTF

In this section, we elaborate on the theory which gives rise to the reduced ZZ rate in the FTF architecture. We specifically consider the level repulsion on the $|101\rangle$ state, as we find it most impacted by the coupling between qubits, and as a result, indicative of how level repulsions affect the ZZ rate as a whole. We will consider the energy shift of the $|101\rangle$ up to 4th order in perturbation theory, where n represents the $|101\rangle$ state, k_i represent any intermediate state that is not n , V_{jk} represents the Hamiltonian matrix element $\langle j | H | k \rangle$ between the two bare states $|j\rangle$, $|k\rangle$, and $E_n^{(m)}$ represents the contribution to the energy of the state $|n\rangle$ at perturbative order m . Energy detunings between two states $|j\rangle$ and $|k\rangle$ are similarly denoted $E_{jk}^{(m)} = E_j^{(m)} - E_k^{(m)}$. In this notation, the 2nd order correction to the energy of $|n\rangle$ is

$$E_n^{(2)} = \sum_{k_1} \frac{|V_{nk_1}|^2}{E_{nk_1}^{(0)}}. \quad (\text{C1})$$

Due to the relatively high energy of the fluxonium $|2\rangle$ states and the transmon $|1\rangle$ state, all intermediate states in this summation have higher energy than $|101\rangle$. The only exception is the $|000\rangle$ state; however, any energy shift involving only states in the computational basis will not contribute to the total ZZ rate because the equal and opposite level repulsions will cancel out when computing ζ . As a result, $E_n^{(2)}$ is negative and independent of the coupler element, provided the computational states are formed by capacitively coupled fluxonium qubits.

To fourth order in perturbation theory, the energy shift is

$$E_n^{(4)} = \sum_{k_1 k_2 k_3} \frac{V_{nk_1} V_{k_1 k_2} V_{k_2 k_3} V_{k_3 n}}{E_{nk_1}^{(0)} E_{nk_2}^{(0)} E_{nk_3}^{(0)}} - E_n^{(2)} \sum_{k_1} \left| \frac{V_{nk_1}}{E_{nk_1}^{(0)}} \right|^2. \quad (\text{C2})$$

While the expression here is more complicated, the qualitative result is the same. Since each energy detuning in the denominators is negative when all intermediate states have higher energy than $|n\rangle$, the resultant quantity $E_n^{(4)}$ is also negative.

Unlike the second and fourth order terms, third order contributions can only exist when both fluxonium qubits are coupled to a third qubit

$$E_n^{(3)} = \sum_{k_1 k_2} \frac{V_{nk_1} V_{k_1 k_2} V_{k_2 n}}{E_{nk_1}^{(0)} E_{nk_2}^{(0)}}. \quad (\text{C3})$$

Contrary to the even-order terms, all third-order contributions are positive, providing the critical mechanism to reduce the ZZ rate. While this analysis has been done just for the energy of the $|101\rangle$ state, numerical computations of Eq. (C1), Eq. (C2), and Eq. (C3) confirm that second and fourth order terms contribute negatively to the overall ZZ , and the third order terms contribute positively to the overall ZZ . In Fig. 8(a), we compute ζ as a function of J_{12} (assuming the optimal corresponding value of J_c) with an exact numerical diagonalization (black) and the aforementioned perturbation theory (red), illustrating that perturbation theory up to 4th order is a sufficient description of the total ZZ rate in the FTF system.

Another interesting feature of FTF unexplored in the main text is that if the transmon frequency is tuned toward infinity, ζ does not return to its value with only the two fluxonium qubits and can in fact decrease even further. In Fig. 8(b), we numerically simulate ζ as a function of the coupler frequency using the Device A parameters and find that ζ asymptotes to less than 10 Hz as the transmon frequency increases. When the transmon frequency is tuned, not only do the energy level detunings increase, but the charge matrix element also increases through the effective E_J . This increase in the charge matrix elements prevents the level repulsions involving the coupler from vanishing even when the coupler frequency becomes infinitely large. This feature makes FTF useful even in fluxonium gate schemes that do not involve the non-computational states. By coupling a fixed frequency transmon (or resonator) with a high frequency (arising from a high E_J) to each fluxonium with the appropriate coupling strengths, ζ can be reduced to near 0 in a robust manner without needing any measurement or calibration of the extra transmon element.

Appendix D: Readout

In our standard readout pulse-sequence [Fig. 9(a)], the qubit and readout pulses were periodically played corresponding to a software trigger, with a fixed wait time τ_1 between the start of the trigger and the start of the readout pulses. The trigger period and τ_1 were chosen such the qubit sufficiently decays to its thermal equilibrium state between measurements.

To initialize the fluxonium qubits in either $|0\rangle$ or $|1\rangle$, we relied on a mostly QND single-shot readout. Then, we post-selected the data for any choice of initial state: $\{|0\rangle, |1\rangle\} \otimes |0\rangle \otimes \{|0\rangle, |1\rangle\}$ in order to herald that state [33]. In our simplest form of post-selection

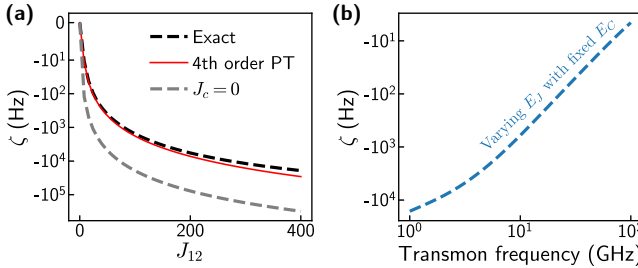


FIG. 8. Numerical simulations of ζ in the FTF system. (a) Plot of ζ along the ‘Minimum ZZ’ parabola in Fig. 2(a), as a function of J_{12} . The black curve shows a numerical diagonalization of the Hamiltonian, which is accurately described by 4th order perturbation theory (red). Without the coupler (gray), $|\zeta|$ is roughly an order of magnitude larger for this range of coupling strengths. (b) Numerical simulation of ζ as a function of the coupler frequency. The Device A parameters from Table I are used, except the effective transmon E_J is changed to vary the transmon frequency. As this frequency increases, $|\zeta|$ decreases asymptotically to below 10 Hz for this set of device parameters.

[Fig. 9(b)], the qubit and readout pulses were played back-to-back with only a short buffer time τ_2 to allow for photons to depopulate the readout resonator prior to the qubit pulses. In our experiment, $\tau_2 = 2 \mu\text{s}$ was much less than the T_1 of any qubit, so the qubits do not return to their thermal equilibrium state by the start of the next pulse sequence. Despite losing a fraction of our data due to this post-selection process, we gain an enormous overhead by not having to wait for the qubits to decay between measurements. Using this method, we obtained typical initialization fidelities between 95% and 99% for $|0\rangle$ and $|1\rangle$ on each qubit. This was calculated as the probability of measuring $|0\rangle$ ($|1\rangle$) if the previous measurement result was also $|0\rangle$ ($|1\rangle$). Due to previously documented non-QND readout effects which transfer population from $|0\rangle$ to $|1\rangle$ [29], the initialization fidelity of the ground state was often 1–2% worse than the excited state.

Ideally, the above method of post-selection would work with the higher-excited states of the fluxonium, but we found in practice that we could not distinguish the $|1\rangle$ and $|2\rangle$ states of the fluxonium in single-shot. To work around this issue, we used a separate two-pulse post-selection technique [Fig. 9(c)]. The first readout initializes the qubit in either $|0\rangle$ or $|1\rangle$, and the second readout records the measurement result. We used the same buffer time τ_2 to avoid measurement-induced dephasing of our qubit and introduced an additional wait time $\tau_3 \sim 50 \mu\text{s}$ to let any population in the non-computational states of the fluxonium to decay to the computational states. Many of our measurements specifically involved driving from $|1\rangle$ to $|2\rangle$ on a particular fluxonium (we include transitions such as $|101\rangle \leftrightarrow |111\rangle$, $|101\rangle \leftrightarrow |102\rangle$, and $|101\rangle \leftrightarrow |201\rangle$ in this discussion). In these cases, we could greatly enhance the readout contrast by performing a π -pulse on each fluxonium prior to readout. After

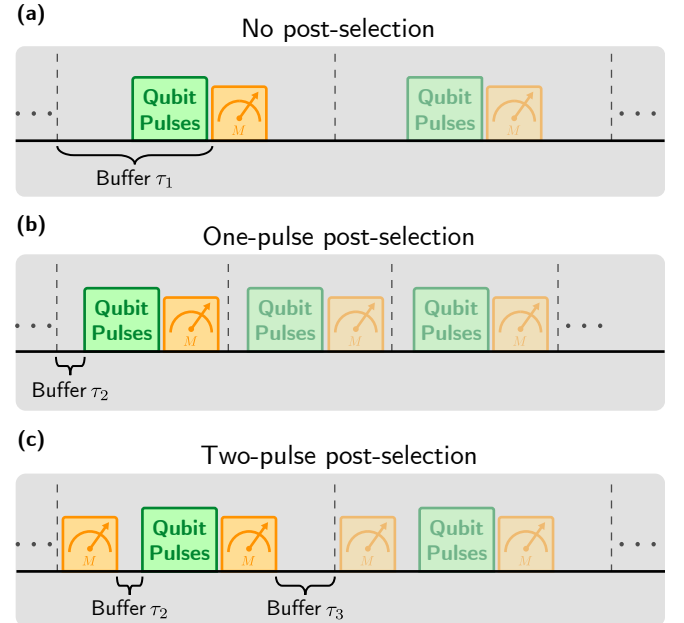


FIG. 9. Pulse diagram for different readout configurations. (a) Standard measurement and readout sequence. Pulses are played on a repeated trigger so that the time between the trigger start and the readout start is kept constant. (b) Single-readout post-selection sequence, also known as heralding. Each readout pulse simultaneously sets the initial state for the subsequent qubit pulses and records the measurement outcome of the previous qubit pulses. To herald the fluxonium ground (excited) state $|0\rangle$ ($|1\rangle$), we only accept measurement results for which the previous readout result was $|0\rangle$ ($|1\rangle$). (c) Two-pulse post-selection (heralding) technique. The first readout is used to initialize the qubit state, and the second is used to measure the result of the qubit pulses. This extra readout pulse allows for an additional buffer time τ_3 without impacting the fidelity of the state preparation.

this π -pulse, any population measured in $|0\rangle$ was assumed to be originally $|1\rangle$, and any population measured in $|1\rangle$ was assumed to be originally $|2\rangle$.

Appendix E: Single-qubit gate calibration

Our single-qubit gates were performed using standard Rabi oscillations using a cosine envelope without a flat top. For the measurements in Fig. 3, we included a 4 ns zero-padding between adjacent pulses. We individually calibrated the X_π pulse and derived all other pulses from it. Y pulses were created by adjusting the phase of the X pulses, pulses differing from π rotation were derived by linearly scaling the pulse amplitude, and Z gates were all implemented as virtual-Z gates. While the set of single-qubit gates could be more carefully calibrated by individually calibrating all other gates, we found our single-qubit gates derived from this process were more than sufficient for accurately calibrating our CZ gate.

We detail the entire calibration sequence used for the X_π gate in Fig. 10, with a flowchart provided in Fig. 10(m). Following an initial rough calibration of the qubit readout, bias voltage, frequency, and π -pulse amplitude, the following procedure was used to precisely calibrate the qubit.

1. Precise sweet-spot calibration [Figs. 10(a, d)].

With fixed drive frequency (slightly negatively detuned from the qubit frequency) and fixed drive amplitude, Ramsey oscillations were obtained as a function of flux around the sweet spot. The oscillation frequencies were fit to a parabola, and the center of the parabola fit was used as the bias voltage corresponding to $\Phi_{\text{ext}} = 0.5 \Phi_0$, termed the ‘sweet spot’.

2. Single-shot readout calibration [Figs. 10(b, e)].

Although optimizing the readout does not impact the gate fidelity, we re-measured the locations of the single-shot blobs corresponding to $|0\rangle$ and $|1\rangle$ here to correct for flux-related changes in the readout signal.

3. Precise qubit frequency calibration

[Figs. 10(c, f)]. To accurately obtain the qubit frequency, we performed qubit spectroscopy with a low enough power such that little power broadening was observed. This typically gave kHz-level precision, a sufficient starting point for DRAG.

4. Derivative Removal by Adiabatic Gate (DRAG) calibration [Figs. 10(g-h, j-k)].

While scanning the DRAG parameter, we performed a train of π -pulses with alternating positive and negative amplitudes. The DRAG parameter which minimized the observed oscillation between the $|0\rangle$ and $|1\rangle$ state was chosen. This measurement may be repeated with a larger number of pulses to increase the resolution of the DRAG parameter. Contrary to other fluxonium experiments [25, 26], we found DRAG calibration necessary to avoid coherent additional errors. We measured the optimal DRAG parameter to vary depending on the room temperature filtering scheme and not with the anharmonicity of the qubit, which leads us to suspect the calibration was correcting for small distortions in the drive line [49].

5. Precise drive amplitude calibration

[Figs. 10(i, l)]. To improve the precision of a single Rabi oscillation, we utilized a pulse train with an odd number of pulses while varying the pulse amplitude. This serves to multiply the oscillation frequency by the number of pulses used, allowing for increased precision on the calibrated π -pulse amplitude.

After calibration, we benchmarked our single-qubit gates using standard single-qubit randomized benchmarking [12, 38]. In our randomized benchmarking, we

applied a sequence of random Clifford gates (decomposed into microwave gates $\{I, \pm X, \pm Y, \pm X_{\pi/2}, \pm Y_{\pi/2}\}$) followed by a recovery gate which inverts the previous sequence and then measure the probability the qubit remains in its initial state (we arbitrarily choose $|0\rangle$). As a function of Clifford sequence length, this probability was fit to the exponential decay: $p_0(m) = Ap^m + B$. In this model, A and B absorb the effects of state preparation and measurement (SPAM) errors, and p is the depolarizing parameter. The average fidelity of each Clifford operation is given by $F_{\text{Clifford}} = 1 - (1 - 1/d)(1 - p)$, where $d = 2^{\text{number of qubits}}$ is the size of the Hilbert space. Our specific decomposition of Clifford gates into microwave single-qubit gates uses, on average, 1.875 gates per Clifford. From this, we compute the average single-qubit gate fidelity as

$$F_{\text{single-qubit}} = 1 - (1 - 1/d)(1 - p)/1.875. \quad (\text{E1})$$

The uncertainty on the fidelity is expressed as a standard error of the mean, which was obtained by setting `absolute_sigma` to be `True` in `scipy.optimize.curve_fit` and using standard error propagation techniques. Error bars on individual RB points are likewise standard errors, obtained by dividing the standard deviation by the square root of the number of randomizations.

Appendix F: Leakage transitions

Driving a single transition in a system of uncoupled qubits is generally equivalent to a single-qubit rotation of some kind. For our CZ gate, such a transition is only entangling provided no other transitions from other initial states are also being driven. This is only possible when coupling terms adjust the energy levels involved in these transitions. To map out the landscape of the relevant higher-level transitions, we performed two-tone spectroscopy as a function of the coupler flux, heralding different initial states: $|000\rangle$, $|100\rangle$, $|001\rangle$, and $|101\rangle$ [Fig. 11]. As demonstrated in the main text, any transition in Fig. 11(d) could be used to perform the CZ gate, provided it is sufficiently detuned from any transitions involving the other initial states. Equivalently, though not explored in this work, a CZ gate could be performed by driving selective transitions from a different initial state and then performing appropriate Z rotations to transfer the 180° conditional phase shift onto the $|1\rangle$ state.

While including a coupler increases the number of parasitic transitions that must be avoided, the larger level repulsions made possible by the coupler increase many relevant detunings. In our devices, many operational points exist where the nearest unwanted transition is more than 100 MHz detuned.

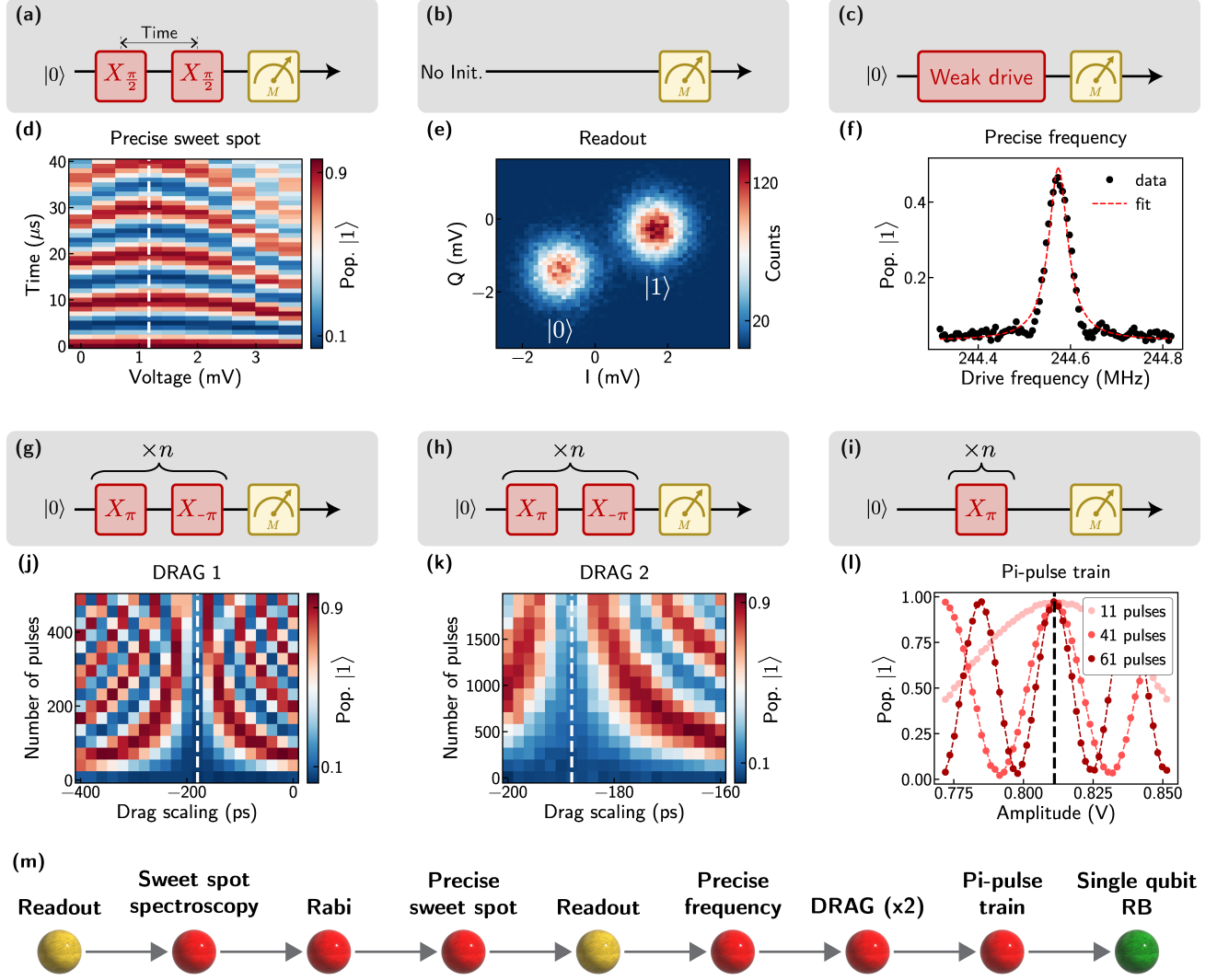


FIG. 10. Single-qubit X_π calibration procedure. (a-c, g-i) Measurement pulse sequences for panels (d-f, j-l) respectively. (d) Ramsey vs. bias voltage measurement in order to precisely determine the voltage corresponding to $\Phi_{\text{ext}} = 0.5 \Phi_0$ (termed the ‘sweet spot’). (e) Calibrating the readout I and Q coordinates for the fluxonium $|0\rangle$ and $|1\rangle$ states. Thermal population of the qubit results in a mixed state prior to readout. (f) Low power spectroscopy of the qubit to precisely determine the qubit frequency. (j) DRAG calibration of the qubit. We played a varying even number of X_π pulses with alternating amplitude while also varying the DRAG parameter. When correctly calibrated, each X_π pulse cancels out with the subsequent $X_{-\pi}$ pulse. (k) A separate DRAG calibration but using a larger number of pulses to calibrate the DRAG parameter more accurately. (l) A pulse train consisting of an odd number of X_π pulses was used to precisely calibrate the amplitude of the pulse. (m) Calibration flowchart for single-qubit gates. Panels are shown for all calibrations starting from the ‘Precise sweet spot’ calibration.

Appendix G: Relative drive amplitude and phase calibration

In this section, we describe a leakage cancellation protocol utilizing destructive interference of the two drives; however, we note that a difference in gate fidelity could not be observed using this method. As a result, for the data in Fig. 4(c), a simpler procedure was implemented to save calibration time: the relative drive phase was tuned to constructively interfere at the desired transition, and the relative amplitudes were kept equal. Despite this

fact, we include the information here for transparency on what was attempted to improve gate fidelities.

In driving our desired transition, off-resonant parasitic transitions always contribute to leakage. With two separate charge drive lines in our device, we can tune each drive line’s relative phase and amplitudes for complete destructive interference on a parasitic transition of our choosing, while retaining a nonzero drive on our gate transition. Without loss of generality, we take $|101\rangle \leftrightarrow |111\rangle$ to be our CZ gate transition and $|100\rangle \leftrightarrow |200\rangle$ to be the closest parasitic transition that we’d like to eliminate. We model the pulse seen by the qubits $i \in \{1, 2\}$

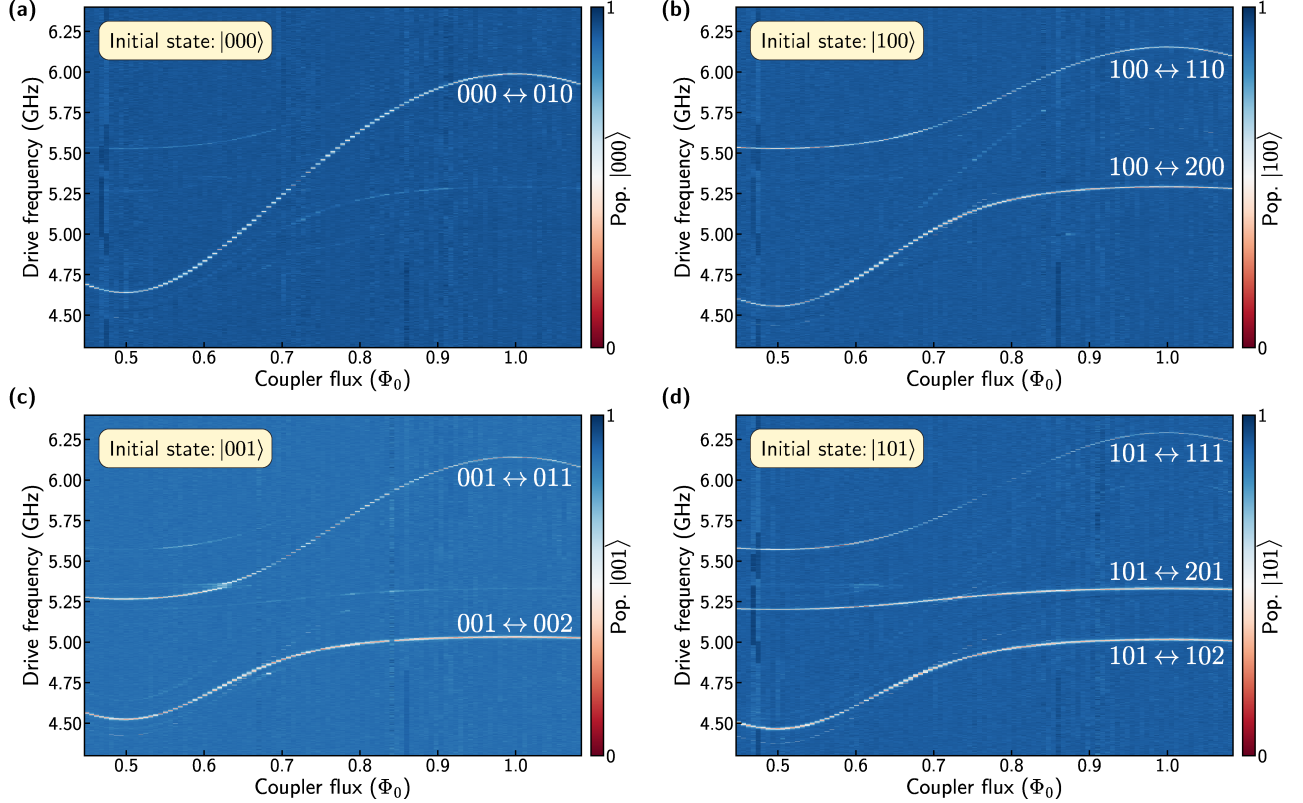


FIG. 11. Two-tone spectroscopy of the higher energy levels of the FTF system. Panels (a-d) consist of the same spectroscopy run post-selecting for $|000\rangle$, $|100\rangle$, $|001\rangle$, or $|101\rangle$ respectively.

as

$$\text{Pulse}_i(t) = A_i \cos(\omega t + kx_i + \phi_i), \quad (\text{G1})$$

where $A_i > 0$ is the pulse amplitude, ω is the angular frequency, k is the wavenumber of the pulse, x_i is the effective distance from each pulse's origin to its destination, and ϕ_i is an additional constant phase offset of each pulse, specified in software.

The Rabi frequency of the undesired transition can then be written as

$$\langle 200 | \hat{H} | 100 \rangle \propto \sum_i A_i \cos(\omega t + kx_i + \phi_i) \langle 200 | \hat{n}_i | 100 \rangle \quad (\text{G2})$$

For this matrix element to be zero for all times, we require the two pulses to be 180° out of phase with each other with equal effective amplitudes. Mathematically, these two conditions are satisfied by specifying the relative phase and amplitude of the two drives:

$$\phi_2 - \phi_1 = \pi - k(x_2 - x_1) \quad (\text{G3})$$

$$\frac{A_2}{A_1} = \frac{\langle 200 | \hat{n}_1 | 100 \rangle}{\langle 200 | \hat{n}_2 | 100 \rangle}, \quad (\text{G4})$$

We note that since $\langle 200 | \hat{n}_1 | 100 \rangle / \langle 200 | \hat{n}_2 | 100 \rangle$ is generally not equal to $\langle 111 | \hat{n}_1 | 101 \rangle / \langle 111 | \hat{n}_2 | 101 \rangle$, these con-

ditions are not expected to provide complete destructive interference on our main transition of interest.

Experimentally, our procedures for calibrating A_2/A_1 and $\phi_2 - \phi_1$ are illustrated in Fig. 12. In all measurements for this calibration, we π -pulsed both fluxonium qubits before readout as discussed in Appendix D to increase signal contrast. We initially started with two arbitrarily amplitudes A_1, A_2 , and then scanned the phase difference $\phi_2 - \phi_1$ (varying ϕ_2 with ϕ_1 fixed) while measuring the $|100\rangle \leftrightarrow |200\rangle$ Rabi oscillation (on resonance) [Figs. 12(a, c)]. With the value of $\phi_2 - \phi_1$ set to minimize the oscillation rate (dashed line), A_2/A_1 was scanned (varying A_2 with A_1 fixed) while measuring the same Rabi oscillation [Figs. 12(b, d)]. The slowest Rabi oscillation (dashed line) was then used to choose the optimal value of A_2/A_1 . Furthermore, as motivated by Eq. (G4), this ratio is independent of frequency and thus didn't require further calibration. On the other hand, we were interested in the phase which caused destructive interference when driving at our two-qubit gate frequency, not at the $|100\rangle \leftrightarrow |200\rangle$ resonance. This required calibrating for the phase dispersion caused by cable length differences. By repeating the relative phase calibration in a frequency bandwidth in which the $|100\rangle \leftrightarrow |200\rangle$ Rabi oscillation was still visible, we uncovered an expected linear dispersion [Fig. 12(e)], which we extrapolated as

a function of drive frequency.

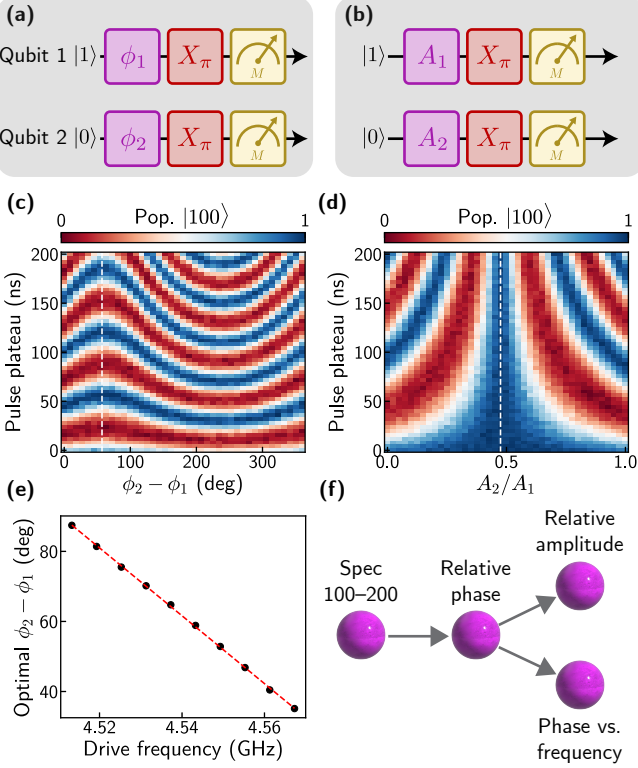


FIG. 12. Relative drive amplitude and phase calibration. (a, b) Pulse sequences for (d-f) respectively. π -pulses before measurement are purely for increasing signal contrast. (c) Rabi oscillation of the unwanted transition with a phase-locked drive on each charge line. The phase difference was scanned to show destructive (white dashed line) and constructive interference. (d) With $\phi_2 - \phi_1$ specified to give destructive interference, the relative amplitudes of the two drives were scanned for *complete* destructive interference (white dashed line). (e) The value of $\phi_2 - \phi_1$ that gave destructive interference was extracted as a function of drive frequency. The linear fit is motivated by a cable length difference. (f) Calibration flowchart for the illustrated procedure.

Appendix H: Two-qubit gate calibration

Prior to a fine calibration of our CZ gate, we would first calibrate single-qubit gates (Appendix E) and the relative drive parameters (Appendix G). Specifically, when calibrating the CZ gate, we increased the pulse width of the single-qubit gates to 50 ns, trading off single-qubit gate fidelities so that coherent errors would not skew our tomography pulses. We also increased the padding between pulses to 10 ns because computational state lifetimes have only a secondary effect on our CZ gate fidelities.

For a given pulse width and gate transition, the remaining four parameters to be calibrated are the drive frequency, overall drive amplitude, and the single-qubit

phase accumulations during our gate interaction. After performing spectroscopy of the transition in interest, we iteratively fine-tuned the drive amplitude and frequency. The drive amplitude was calibrated by performing a simple Rabi oscillation and minimizing the leakage [Figs. 13(a, d)]. According to our error budget outlined in Appendix K, a single CZ pulse yields a sufficiently precise calibration. The drive frequency was calibrated by performing a Ramsey-like measurement on qubit 1 to measure its phase accrual after a pulse-train of CZ gates, depending on whether or not qubit 2 started in $|0\rangle$ or $|1\rangle$ [Figs. 13(b, e)]. The difference in this phase accrual was tuned to be 180° , though we note that controlled-phase gates of variable angles could also be achieved. Since adjusting the drive frequency slightly changes the amplitude corresponding to a single period and vice-versa, we alternately performed these two calibrations three times in total. In practice, we found this was sufficiently accurate and much faster than performing a two-dimensional calibration for both parameters simultaneously. Finally, once the CZ interaction was properly tuned, we measured the single-qubit phase accumulation during the CZ interaction using the same Ramsey-like measurement [Figs. 13(c, f)]. These Z-rotations were corrected for in software through virtual-Z gates. We illustrate the complete flowchart of this calibration in Fig. 13(g).

To benchmark our CZ gate, we performed two-qubit interleaved randomized benchmarking, in which Clifford gates were sampled from the two-qubit Clifford group, generated by $\{I, \pm X, \pm Y, \pm X_{\pi/2}, \pm Y_{\pi/2}, \text{CZ}\}$. Our specific decomposition results in 8.25 single-qubit gates and 1.5 CZ gates per Clifford.

Interleaved randomized benchmarking consists of two steps: (1) performing standard randomized benchmarking, in which we extract the depolarizing parameter by measuring sequence fidelity with initial state $|00\rangle$ and fitting to the decay $p_{00} = Ap^m + B$. (2) Performing the same standard randomization benchmarking sequence, except an additional CZ gate is inserted between each pair of Cliffords, and the final recovery gate is modified accordingly. Fitting this decay gives p_{int} , the interleaved depolarizing parameter. By comparing the relative decays between the two steps, the average CZ gate fidelity is extracted as

$$F_{\text{CZ}} = 1 - (d - 1)(1 - p_{\text{int}}/p)/d, \quad (\text{H1})$$

and its uncertainty is once again represented as a standard error, following the procedure of Appendix E.

Appendix I: Reinforcement learning

As described in the main text, we used a model-free reinforcement learning agent to boost the gate fidelity beyond the physics-based calibration described in the previous section. Specifically, we used an algorithm known as proximal policy optimization (PPO).

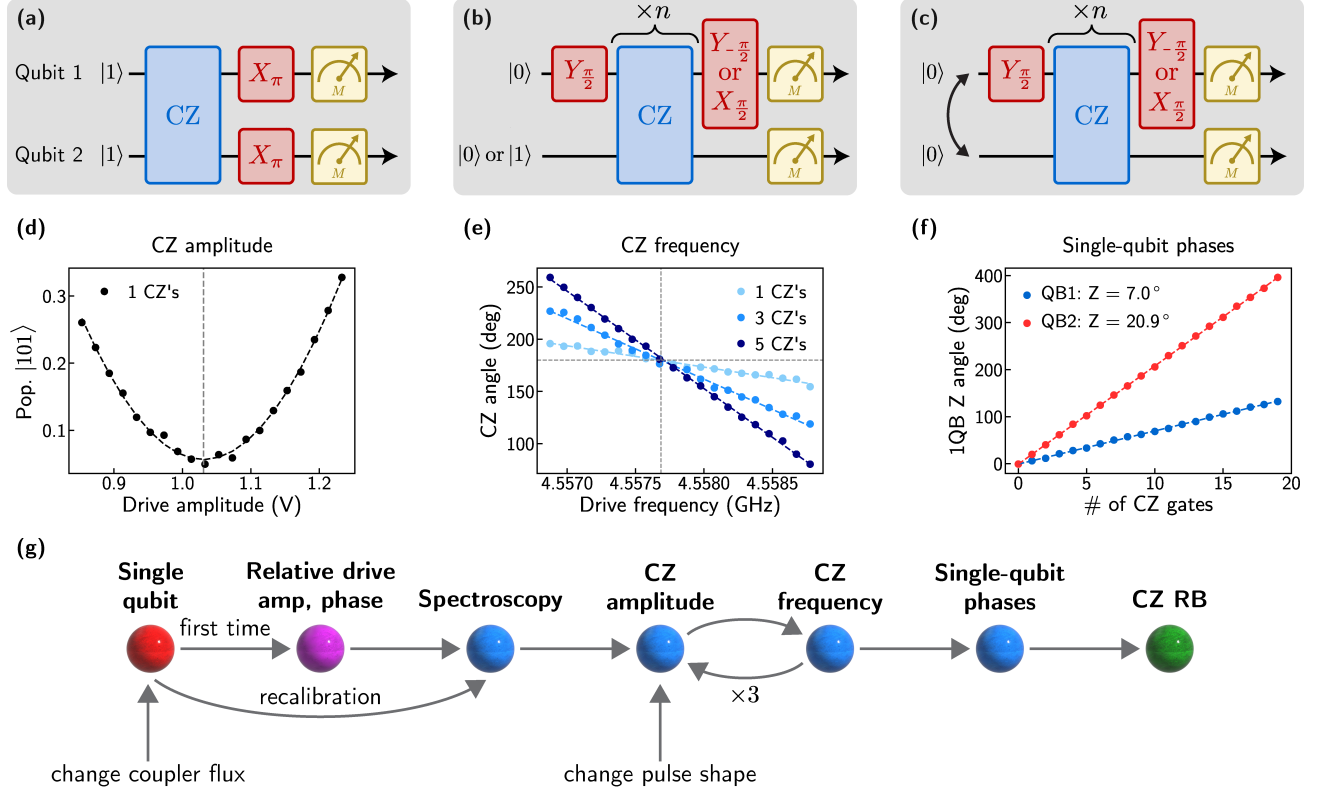


FIG. 13. **CZ Gate calibration procedure.** (a-c) Pulse sequences for (d-f) respectively. The double arrow in (c) indicates that the same pulse sequence was performed twice, with qubits 1 and 2 exchanged. (d) Calibrating the global amplitude of the CZ drive by minimizing the leakage. (e) Calibrating the frequency of the CZ drive by measuring a conditional phase accumulation via Ramsey-like measurements. Each gate should contribute a 180° conditional phase shift. (f) Measuring the single-qubit phase accumulations per CZ gate using the same Ramsey-like measurements. (g) Graphical illustration of the full two-qubit calibration routine. When recalibrating the system for small flux drifts or periodic check-ins, we found it unnecessary to recalibrate the relative drive amplitude or phase.

Application of reinforcement learning to quantum control has been discussed in detail in the literature. Here, we closely followed the procedure discussed in [46] and implemented in [50], with code adapted from [51] and built on TF-Agents. As seen in Fig. 5(b-c), each round of training used 300 epochs and lasted roughly 75 minutes. We found the ~ 15 second training time per epoch to be almost completely dominated by AWG waveform upload time, which took over 12 seconds for the data shown in Fig. 5. As updating the agent’s policy according to PPO took comparably less time (less than 1 second), we elected to simply run PPO on the measurement computer instead of, for example, a separate computer equipped with a GPU. Since averaging was also relatively inexpensive compared to pulse upload time, we also elected to average the measurement results for each trial pulse 1000 times.

TABLE III. **Reinforcement learning parameters.** Hyper-parameters of the PPO algorithm used to optimize the CZ gate.

Learning rate	0.01
Number of policy updates	20
Importance ratio clipping	0.1
Batch size	30
Number of averages	1000
Value prediction loss coefficient	0.005
Gradient clipping	1.0
Log probability clipping	0.0

Appendix J: CZ Gate vs. flux

Figure 14 shows an alternate plotting of the data in Fig. 4(c), illustrating more explicitly what frequencies each calibrated gate corresponds to. As mentioned in the main text, each plot was created from a fully-automated measurement across 21 linearly spaced values of the coupler flux. While many calibrated points have low fidelity, the most important aspect of this architecture is that

there exist multiple transitions for which high fidelity is achievable, allowing flexibility in the operation frequency. Nevertheless, we discuss the most common failure mechanisms and reasons for low fidelity to shed additional insights on the limits of our automated calibration versus the inherent limit of the transition being driven.

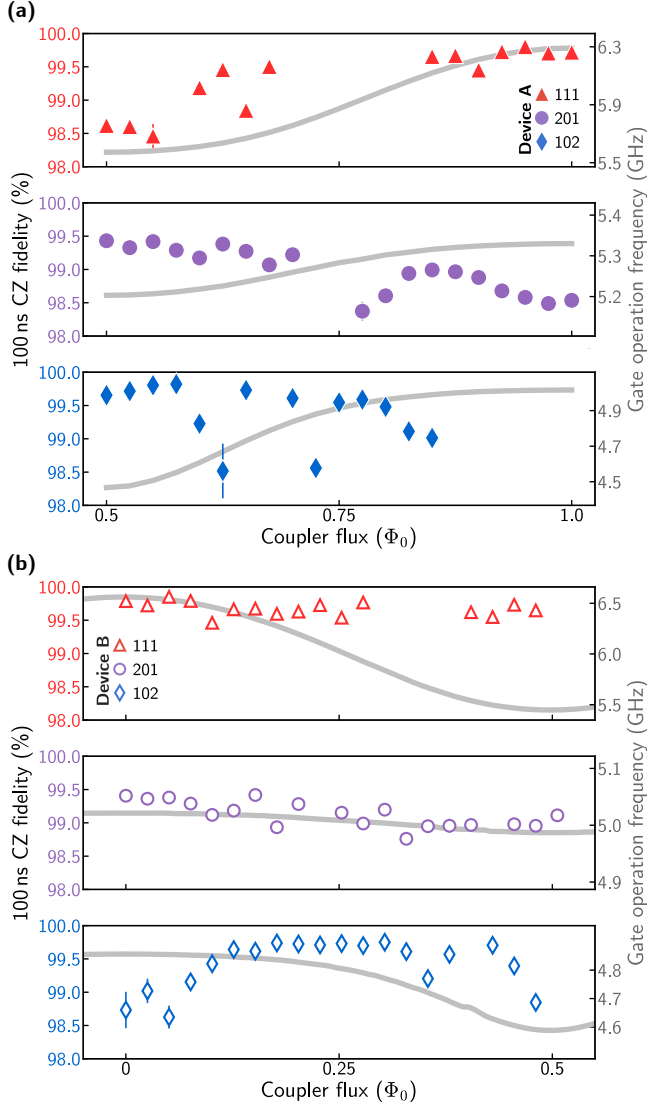


FIG. 14. Alternate plotting of the data in Fig. 4(c). Gate fidelities with a fixed 100 ns pulse width as a function of the coupler flux for Device A (a) and Device B (b). The drive frequency is plotted in gray, represented on the right axis. All points missing from the full set of 21 correspond to more severe calibration failures.

The most common reason for low-performance operation points was nearby unwanted transitions, leading to a high amount of leakage. This is most evident in Device A, in which the $|101\rangle \leftrightarrow |111\rangle$ transition at $\Phi_{\text{ext},c} = 1.0 \Phi_0$, and the $|101\rangle \leftrightarrow |102\rangle$ transition at $\Phi_{\text{ext},c} = 0.5 \Phi_0$ are furthest detuned from their nearest unwanted transition, resulting in higher fidelities in these regions. Where these

unwanted transitions have a much smaller detuning, we expect to obtain higher fidelities by increasing the drive pulse beyond 100 ns. In other regions, we expect higher fidelities by decreasing the gate time.

A second common mechanism for failed calibration was the inability to find a drive frequency corresponding to a 180° conditional phase shift. Due to the large hybridization, we occasionally measured ac-Stark shifts large enough to counter-balance the natural change in the conditional-phase angle as a function of drive detuning. The calibration could be recovered by either using a slower gate or by adjusting the relative drive amplitudes to tweak the total ac-stark shift.

Other less common mechanisms for a failed calibration include TLSs or accidental resonances with undesired transitions, including higher-photon transitions.

Figure 15 shows the individual qubit coherence times as a function of the local coupler flux in Device A. Each coherence time was simultaneously measured on each qubit, with both qubits precisely re-tuned to $\Phi_{\text{ext}} = 0.5 \Phi_0$ for each value of the coupler flux. Notably, these coherence times are slightly shorter than those listed in Table I, due to bias-induced heating of the local flux lines. However, these coherence times are a more accurate representation of the quality of the qubits when performing two-qubit gates and simultaneous single-qubit gates. When performing simultaneous single-qubit gates, we biased the coupler at roughly $\Phi_{\text{ext},c} = 0.77 \Phi_0$, corresponding to no current being sent through the coupler flux line. We suspect the low Ramsey time of qubit 2 to be caused by Aharonov-Casher dephasing from coherent quantum phase slips [52, 53], based on its Hamiltonian parameters.

Appendix K: Error modeling

In this section, we build up an analytic error budget to estimate the impact of various types of coherent and incoherent errors on gate fidelities. We model our gates as a completely positive trace-preserving (in some subspace) map \mathcal{G} acting on an input state ρ . The Kraus representation theorem then allows us to express all such processes as $\mathcal{G}(\rho) = \sum_k G_k \rho G_k^\dagger$ for some set of Kraus operators G_k obeying the normalization condition $\sum_k G_k^\dagger G_k = I$. The average state fidelity of such a process \mathcal{G} is then given by

$$F = \frac{1}{n(n+1)} \left[\text{Tr} \left(\sum_k M_k^\dagger M_k \right) + \sum_k |\text{Tr}(M_k)|^2 \right], \quad (\text{K1})$$

where $M_k = PU_0^\dagger G_k P$, and n is the dimension of the computational subspace [54]. Also, P is the projection operator onto the computational subspace, and U_0 is the ideal unitary operation of the process. We reproduce here the error corresponding to relaxation (T_1) and pure (Markovian) dephasing (T_ϕ) corresponding to a gate of

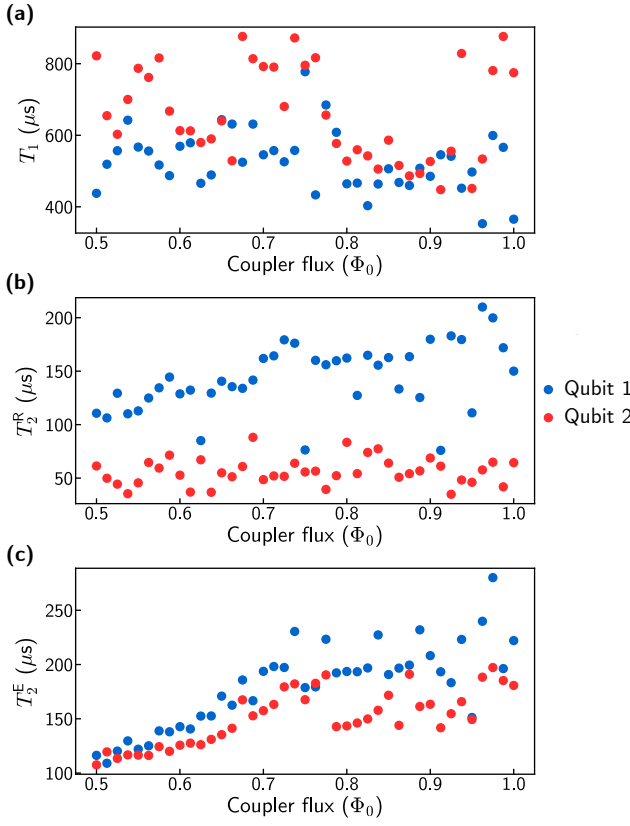


FIG. 15. **Qubit coherences in Device A with both qubits biased at $0.5\Phi_0$.** Panels (a), (b), (c) show the T_1 , Ramsey, and echo decay times respectively as a function of the coupler flux. All decays were fit to an exponential and measurements were performed over a 12 hour period.

length t_g .

$$F_{1 \text{ qubit}} = 1 - \frac{t_g}{3} \left(\frac{1}{T_1} + \frac{1}{T_\phi} \right) \quad (\text{K2})$$

$$F_{2 \text{ qubits}} = 1 - \frac{4t_g}{5} \left(\frac{1}{T_1} + \frac{1}{T_\phi} \right) \quad (\text{K3})$$

One critical assumption in these well-known formulas is that the gate operation stays within the computational subspace, an invalid assumption for our two-qubit gate.

1. Relaxation of higher energy levels

In our two-qubit gate, there are five relevant states: the computational states $\{|00\rangle, |01\rangle, |10\rangle, |11\rangle\}$ and the non-computational state we drive to $|\alpha\rangle$. For mathematical simplicity, we imagine modeling an identity gate composed of two CZ gates. The error per unit time will not change, and this allows us to use $U_0 = I$ as well as simplifies the phases in our Kraus operators. We model the incoherent decay under driven evolution as if $|11\rangle$ and $|\alpha\rangle$

decay into each other at equivalent rates (a valid assumption when the gate time t_g is small compared to the relaxation rate $T_{1,\alpha}$). Assuming no other decay channels, the full set of Kraus operators for this process is

$$G_0 = \frac{1}{\sqrt{2}} \begin{pmatrix} 1 & 0 & 0 & 0 & 0 \\ 0 & 1 & 0 & 0 & 0 \\ 0 & 0 & 1 & 0 & 0 \\ 0 & 0 & 0 & 1 & 0 \\ 0 & 0 & 0 & 0 & e^{-t/2T_1} \end{pmatrix} \quad (\text{K4})$$

$$G_1 = \frac{1}{\sqrt{2}} \begin{pmatrix} 0 & 0 & 0 & 0 & 0 \\ 0 & 0 & 0 & 0 & 0 \\ 0 & 0 & 0 & 0 & 0 \\ 0 & 0 & 0 & 0 & \sqrt{1 - e^{-t/T_1}} \\ 0 & 0 & 0 & 0 & 0 \end{pmatrix} \quad (\text{K5})$$

$$G_2 = \frac{1}{\sqrt{2}} \begin{pmatrix} 1 & 0 & 0 & 0 & 0 \\ 0 & 1 & 0 & 0 & 0 \\ 0 & 0 & 1 & 0 & 0 \\ 0 & 0 & 0 & e^{-t/2T_1} & 0 \\ 0 & 0 & 0 & 0 & 1 \end{pmatrix} \quad (\text{K6})$$

$$G_3 = \frac{1}{\sqrt{2}} \begin{pmatrix} 0 & 0 & 0 & 0 & 0 \\ 0 & 0 & 0 & 0 & 0 \\ 0 & 0 & 0 & 0 & 0 \\ 0 & 0 & 0 & 0 & 0 \\ 0 & 0 & 0 & \sqrt{1 - e^{-t/T_1}} & 0 \end{pmatrix} \quad (\text{K7})$$

One can verify the behavior of these operators by computing that $\langle 11 | \mathcal{G}(\rho) | 11 \rangle = \frac{\rho_{11} + \rho_\alpha}{2} + \frac{\rho_{11} - \rho_\alpha}{2} e^{-t/T_{1,\alpha}}$. Finally, we take the projection operator to be $P = |00\rangle\langle 00| + |01\rangle\langle 01| + |10\rangle\langle 10| + |11\rangle\langle 11|$. Inserting these operators into Eq. (K1) and Taylor expanding in $t_g/T_{1,\alpha} < 1$, we obtain

$$F \approx 1 - \frac{1}{8} \frac{t_g}{T_{1,\alpha}}. \quad (\text{K8})$$

2. CZ phase error

We consider an error in phase calibration, in which we successfully return all population back to the computational subspace, but with a $|11\rangle$ state phase of $\pi + d\phi$. In the unitary special case of Eq. (K1) ($\mathcal{G}(\rho) = U\rho U^\dagger$), we need only compute

$$M = U_0^\dagger U \quad (\text{K9})$$

$$= \begin{bmatrix} 1 & 0 & 0 & 0 \\ 0 & 1 & 0 & 0 \\ 0 & 0 & 1 & 0 \\ 0 & 0 & 0 & -1 \end{bmatrix} \begin{bmatrix} 1 & 0 & 0 & 0 \\ 0 & 1 & 0 & 0 \\ 0 & 0 & 1 & 0 \\ 0 & 0 & 0 & e^{-i\pi - id\phi} \end{bmatrix} \quad (\text{K10})$$

$$= \begin{bmatrix} 1 & 0 & 0 & 0 \\ 0 & 1 & 0 & 0 \\ 0 & 0 & 1 & 0 \\ 0 & 0 & 0 & e^{-id\phi} \end{bmatrix}. \quad (\text{K11})$$

Inserting this into Eq. (K1), we obtain

$$F = \frac{7 + 3 \cos(d\phi)}{10} \approx 1 - \frac{3}{20} d\phi^2. \quad (\text{K12})$$

Values of note are that for a fidelity of 99.9%, we can tolerate a phase error of 4.7° and for a fidelity of 99.99%, we can tolerate a phase error of 1.5° . We can similarly convert this into an error on drive frequency, assuming the drive frequency is the sole degree of freedom in tuning the aforementioned phase. The geometric phase accumulation associated with some frequency change δ of a full-period driven oscillation is $\delta t_g/2$. The angle errors above then translate into 0.5 MHz error for 99.9% fidelity and 160 kHz for 99.99% fidelity.

3. Amplitude error

In calibrating the Rabi oscillation driving our CZ gate, we chose a fixed gate time and calibrated the amplitude of the pulse to obtain a single-period oscillation. The unitary corresponding to this Rabi rotation in our five-state Hilbert space $\{|00\rangle, |01\rangle, |10\rangle, |11\rangle, |\alpha\rangle\}$ is

$$U = \begin{pmatrix} 1 & 0 & 0 & 0 & 0 \\ 0 & 1 & 0 & 0 & 0 \\ 0 & 0 & 1 & 0 & 0 \\ 0 & 0 & 0 & \cos(\Omega t/2) & -i \sin(\Omega t/2) \\ 0 & 0 & 0 & -i \sin(\Omega t/2) & \cos(\Omega t/2) \end{pmatrix} \quad (\text{K13})$$

where Ω is the Rabi oscillation of the CZ pulse. Projecting onto the computational subspace (P) and assuming an ideal CZ unitary

$$U_0 = |00\rangle\langle 00| + |01\rangle\langle 01| + |10\rangle\langle 10| - |11\rangle\langle 11|, \quad (\text{K14})$$

we insert $M = PU_0^\dagger UP$ into Eq. (K1) to obtain

$$F = \frac{1}{10}(6 - 3 \cos(\Omega t/2) + \cos^2(\Omega t/2)) \approx 1 - \frac{1}{16} d\theta^2. \quad (\text{K15})$$

Converting this amplitude error into a phase error $d\theta = \Omega t - 2\pi$, 99.9% fidelity corresponds to a 7.25° error and 99.99% fidelity corresponds to a 2.29° error. To relate this more directly to our experimental apparatus, assuming that the pulse is calibrated to a roughly 1 V amplitude, these phases correspond to voltage errors of 20 mV and 6.4 mV respectively.

We conclude this section by emphasizing that at the error levels discussed, calibration precision is quite lenient and that errors will be dominated by decoherence and other unmodeled behavior such as leakage through neighboring transitions. Furthermore, all calculations performed are meant to model the fidelity of a single-gate, which may not necessarily be equal to the fidelity extracted from interleaved randomized benchmarking due to the nature of coherent errors.

Appendix L: Device B

In this section, we show data corresponding to Device B, a secondary device. Device B is an identically designed device, with extracted Hamiltonian parameters varying by up to 10% as compared to Device A, typical of fabrication variations and differences in device aging. The coherence times and single-qubit gate fidelities remain consistently high across both devices, and in particular, fluxonium 2 on Device B exhibited a median T_1 of 1.26 ms averaged over 9 hours [see Fig. 16(a)]. This, along with the measured lifetimes of fluxonium 2 on Device A, points to a reliable process and design for achieving high lifetime qubits in a planar geometry. Curiously, the single-qubit gate fidelities in Fig. 16(b) were found to be optimized near a pulse width of 50 ns, a significant difference between the optimal pulse width of 18 ns for Device A. We currently do not have an explanation for this discrepancy.

We measured a nearly identical value (within 1 kHz) of the ZZ interaction rate in this device [Fig. 16(c)], supporting our claim that the ZZ reduction does not rely on any precise parameter matching and is a reliable method to achieve (absolute) values below 10 kHz. Most importantly, despite changes of up to 300 MHz in the $|1\rangle \leftrightarrow |2\rangle$ transition frequencies of the fluxonium qubits, we could still demonstrate high-fidelity CZ gates across a large frequency range [see Fig. 4(c) in the main text], with peak fidelities above 99.8% [see Figs. 16(d-f)].

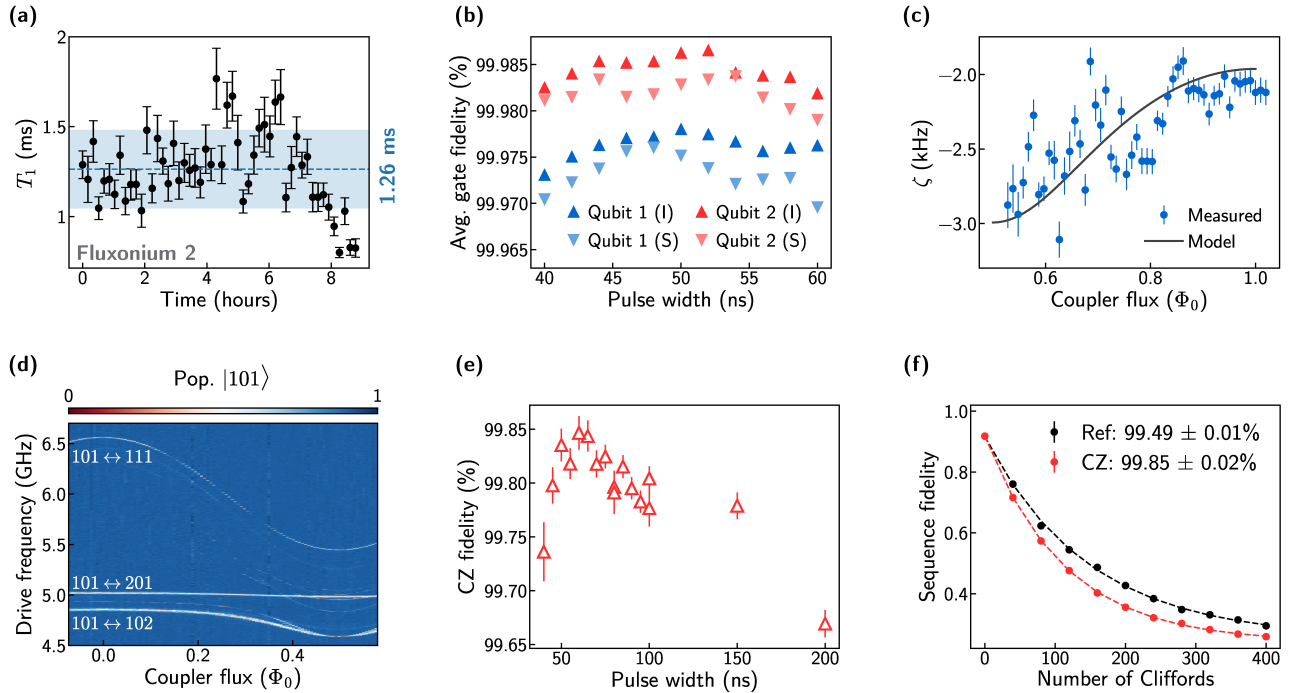


FIG. 16. **Selected data from Device B.** (a) Repeated T_1 measurements of fluxonium 2 over a roughly nine-hour time span. The dashed blue line indicates the median T_1 of 1.26 ms, and the blue shaded region encompasses ± 1 standard deviations. (b) Individual (I) and simultaneous (S) randomized benchmarking for both qubits, varying the width of a cosine pulse envelope. (c) Measured ZZ-interaction strength as a function of the coupler flux. (d) Spectroscopy of the non-computational states which activate the two-qubit gate. (e) CZ fidelities with varying pulse width, driving the $|101\rangle \leftrightarrow |111\rangle$ transition at $\Phi_{\text{ext},c} = 0.063$. (f) Reference and interleaved randomized benchmarking traces averaged over 20 randomizations for a pulse width of 60 ns.

- [1] Y. Nakamura, Y. A. Pashkin, and J. S. Tsai, Coherent control of macroscopic quantum states in a single-cooper-pair box, *Nature* **398**, 786 (1999).
- [2] L. B. Ioffe, V. B. Geshkenbein, M. V. Feigel'Man, A. L. Fauchere, and G. Blatter, Environmentally decoupled sds-wave josephson junctions for quantum computing, *Nature* **398**, 679 (1999).
- [3] J. Mooij, T. Orlando, L. Levitov, L. Tian, C. H. Van der Wal, and S. Lloyd, Josephson persistent-current qubit, *Science* **285**, 1036 (1999).
- [4] J. Koch, M. Y. Terri, J. Gambetta, A. A. Houck, D. Schuster, J. Majer, A. Blais, M. H. Devoret, S. M. Girvin, and R. J. Schoelkopf, Charge-insensitive qubit design derived from the cooper pair box, *Phys. Rev. A* **76**, 042319 (2007).
- [5] V. E. Manucharyan, J. Koch, L. I. Glazman, and M. H. Devoret, Fluxonium: Single cooper-pair circuit free of charge offsets, *Science* **326**, 113 (2009).
- [6] F. Yan, S. Gustavsson, A. Kamal, J. Birenbaum, A. P. Sears, D. Hover, T. J. Gudmundsen, D. Rosenberg, G. Samach, S. Weber, *et al.*, The flux qubit revisited to enhance coherence and reproducibility, *Nature Communications* **7**, 1 (2016).
- [7] A. Gyenis, P. S. Mundada, A. Di Paolo, T. M. Hazard, X. You, D. I. Schuster, J. Koch, A. Blais, and A. A. Houck, Experimental realization of a protected superconducting circuit derived from the $0-\pi$ qubit, *PRX Quantum* **2**, 010339 (2021).
- [8] J. Majer, J. Chow, J. Gambetta, J. Koch, B. Johnson, J. Schreier, L. Frunzio, D. Schuster, A. A. Houck, A. Wallraff, *et al.*, Coupling superconducting qubits via a cavity bus, *Nature* **449**, 443 (2007).
- [9] C. Rigetti and M. Devoret, Fully microwave-tunable universal gates in superconducting qubits with linear couplings and fixed transition frequencies, *Phys. Rev. B* **81**, 134507 (2010).
- [10] S. Poletto, J. M. Gambetta, S. T. Merkel, J. A. Smolin, J. M. Chow, A. Córcoles, G. A. Keefe, M. B. Rothwell, J. Rozen, D. Abraham, *et al.*, Entanglement of two superconducting qubits in a waveguide cavity via monochromatic two-photon excitation, *Phys. Rev. Lett.* **109**, 240505 (2012).
- [11] J. M. Chow, J. M. Gambetta, A. W. Cross, S. T. Merkel, C. Rigetti, and M. Steffen, Microwave-activated conditional-phase gate for superconducting qubits, *New Journal of Physics* **15**, 115012 (2013).
- [12] R. Barends, J. Kelly, A. Megrant, A. Veitia, D. Sank, E. Jeffrey, T. C. White, J. Mutus, A. G. Fowler, B. Campbell, *et al.*, Superconducting quantum circuits at the surface code threshold for fault tolerance, *Nature* **508**, 500 (2014).
- [13] M. Reagor, C. B. Osborn, N. Tezak, A. Staley, G. Prawiroatmodjo, M. Scheer, N. Alidoust, E. A. Sete, N. Didier, M. P. da Silva, *et al.*, Demonstration of universal parametric entangling gates on a multi-qubit lattice, *Science Advances* **4**, eaao3603 (2018).
- [14] D. L. Campbell, Y.-P. Shim, B. Kannan, R. Winik, D. K. Kim, A. Melville, B. M. Niedzielski, J. L. Yoder, C. Tahan, S. Gustavsson, and W. D. Oliver, Universal nonadiabatic control of small-gap superconducting qubits, *Phys. Rev. X* **10**, 041051 (2020).
- [15] H. Zhang, S. Chakram, T. Roy, N. Earnest, Y. Lu, Z. Huang, D. Weiss, J. Koch, and D. I. Schuster, Universal fast-flux control of a coherent, low-frequency qubit, *Phys. Rev. X* **11**, 011010 (2021).
- [16] Y. Sung, L. Ding, J. Braumüller, A. Vepsäläinen, B. Kannan, M. Kjaergaard, A. Greene, G. O. Samach, C. McNally, D. Kim, *et al.*, Realization of high-fidelity cz and zz-free iswap gates with a tunable coupler, *Phys. Rev. X* **11**, 021058 (2021).
- [17] F. Yan, P. Krantz, Y. Sung, M. Kjaergaard, D. L. Campbell, T. P. Orlando, S. Gustavsson, and W. D. Oliver, Tunable coupling scheme for implementing high-fidelity two-qubit gates, *Phys. Rev. Applied* **10**, 054062 (2018).
- [18] F. Arute, K. Arya, R. Babbush, D. Bacon, J. C. Bardin, R. Barends, R. Biswas, S. Boixo, F. G. Brandao, D. A. Buell, *et al.*, Quantum supremacy using a programmable superconducting processor, *Nature* **574**, 505 (2019).
- [19] R. Acharya, I. Aleiner, R. Allen, T. I. Andersen, M. Ansmann, F. Arute, K. Arya, A. Asfaw, J. Atalaya, R. Babbush, *et al.*, Suppressing quantum errors by scaling a surface code logical qubit, *Nature* **614**, 676 (2023).
- [20] W. Smith, A. Kou, X. Xiao, U. Vool, and M. Devoret, Superconducting circuit protected by two-cooper-pair tunneling, *npj Quantum Information* **6**, 8 (2020).
- [21] N. Earnest, S. Chakram, Y. Lu, N. Irons, R. K. Naik, N. Leung, L. Ocola, D. A. Czaplewski, B. Baker, J. Lawrence, J. Koch, and D. I. Schuster, Realization of a Λ system with metastable states of a capacitively shunted fluxonium, *Phys. Rev. Lett.* **120**, 150504 (2018).
- [22] L. B. Nguyen, Y.-H. Lin, A. Somoroff, R. Mencia, N. Grabon, and V. E. Manucharyan, High-coherence fluxonium qubit, *Phys. Rev. X* **9**, 041041 (2019).
- [23] L. B. Nguyen, G. Koolstra, Y. Kim, A. Morvan, T. Chistolini, S. Singh, K. N. Nesterov, C. Jünger, L. Chen, Z. Pedramrazi, B. K. Mitchell, J. M. Kreikebaum, S. Puri, D. I. Santiago, and I. Siddiqi, Blueprint for a high-performance fluxonium quantum processor, *PRX Quantum* **3**, 037001 (2022).
- [24] I. M. Pop, K. Geerlings, G. Catelani, R. J. Schoelkopf, L. I. Glazman, and M. H. Devoret, Coherent suppression of electromagnetic dissipation due to superconducting quasiparticles., *Nature* **508**, 369 (2014).
- [25] A. Somoroff, Q. Ficheux, R. A. Mencia, H. Xiong, R. V. Kuzmin, and V. E. Manucharyan, Millisecond coherence in a superconducting qubit, *arXiv preprint arXiv:2103.08578* (2021).
- [26] F. Bao, H. Deng, D. Ding, R. Gao, X. Gao, C. Huang, X. Jiang, H.-S. Ku, Z. Li, X. Ma, *et al.*, Fluxonium: an alternative qubit platform for high-fidelity operations, *Phys. Rev. Lett.* **129**, 010502 (2022).
- [27] E. Dogan, D. Rosenstock, L. L. Guevel, H. Xiong, R. A. Mencia, A. Somoroff, K. N. Nesterov, M. G. Vavilov, V. E. Manucharyan, and C. Wang, Demonstration of the two-fluxonium cross-resonance gate, *arXiv preprint arXiv:2204.11829* (2022).
- [28] I. N. Moskalenko, I. A. Simakov, N. N. Abramov, D. O. Moskalev, A. A. Pishchimova, N. S. Smirnov, E. V. Zikiy, I. A. Rodionov, and I. S. Besedin, High fidelity two-qubit gates on fluxoniums using a tunable coupler, *npj Quantum Information* **8** (2022).
- [29] Q. Ficheux, L. B. Nguyen, A. Somoroff, H. Xiong, K. N.

- Nesterov, M. G. Vavilov, and V. E. Manucharyan, Fast logic with slow qubits: microwave-activated controlled-z gate on low-frequency fluxoniums, *Phys. Rev. X* **11**, 021026 (2021).
- [30] H. Xiong, Q. Ficheux, A. Somoroff, L. B. Nguyen, E. Dogan, D. Rosenstock, C. Wang, K. N. Nesterov, M. G. Vavilov, and V. E. Manucharyan, Arbitrary controlled-phase gate on fluxonium qubits using differential ac stark shifts, *Phys. Rev. Research* **4**, 023040 (2022).
- [31] S. Sheldon, E. Magesan, J. M. Chow, and J. M. Gambetta, Procedure for systematically tuning up cross-talk in the cross-resonance gate, *Phys. Rev. A* **93**, 060302 (2016).
- [32] J. B. Hertzberg, E. J. Zhang, S. Rosenblatt, E. Magesan, J. A. Smolin, J.-B. Yau, V. P. Adiga, M. Sandberg, M. Brink, J. M. Chow, *et al.*, Laser-annealing josephson junctions for yielding scaled-up superconducting quantum processors, *npj Quantum Information* **7**, 1 (2021).
- [33] J. Johnson, C. Macklin, D. Slichter, R. Vijay, E. Weingarten, J. Clarke, and I. Siddiqi, Heralded state preparation in a superconducting qubit, *Phys. Rev. Lett.* **109**, 050506 (2012).
- [34] E. A. Sete, J. M. Martinis, and A. N. Korotkov, Quantum theory of a bandpass purcell filter for qubit readout, *Phys. Rev. A* **92**, 012325 (2015).
- [35] F. Setiawan, P. Groszkowski, H. Ribeiro, and A. A. Clerk, Analytic design of accelerated adiabatic gates in realistic qubits: General theory and applications to superconducting circuits, *PRX Quantum* **2**, 030306 (2021).
- [36] F. Setiawan, P. Groszkowski, and A. A. Clerk, Fast and robust geometric two-qubit gates for superconducting qubits and beyond, *Phys. Rev. Appl.* **19**, 034071 (2023).
- [37] P. S. Mundada, A. Gyenis, Z. Huang, J. Koch, and A. A. Houck, Floquet-engineered enhancement of coherence times in a driven fluxonium qubit, *Phys. Rev. Applied* **14**, 054033 (2020).
- [38] E. Magesan, J. M. Gambetta, and J. Emerson, Scalable and robust randomized benchmarking of quantum processes, *Phys. Rev. Lett.* **106**, 180504 (2011).
- [39] D. C. McKay, C. J. Wood, S. Sheldon, J. M. Chow, and J. M. Gambetta, Efficient z gates for quantum computing, *Phys. Rev. A* **96**, 022330 (2017).
- [40] A. D. Córcoles, J. M. Gambetta, J. M. Chow, J. A. Smolin, M. Ware, J. Strand, B. L. Plourde, and M. Steffen, Process verification of two-qubit quantum gates by randomized benchmarking, *Phys. Rev. A* **87**, 030301 (2013).
- [41] E. Magesan, J. M. Gambetta, B. R. Johnson, C. A. Ryan, J. M. Chow, S. T. Merkel, M. P. Da Silva, G. A. Keefe, M. B. Rothwell, T. A. Ohki, *et al.*, Efficient measurement of quantum gate error by interleaved randomized benchmarking, *Phys. Rev. Lett.* **109**, 080505 (2012).
- [42] J. Schulman, F. Wolski, P. Dhariwal, A. Radford, and O. Klimov, Proximal policy optimization algorithms, *CoRR* **abs/1707.06347** (2017), 1707.06347.
- [43] Z. An and D. Zhou, Deep reinforcement learning for quantum gate control, *Europhysics Letters* **126**, 60002 (2019).
- [44] M. Y. Niu, S. Boixo, V. N. Smelyanskiy, and H. Neven, Universal quantum control through deep reinforcement learning, *npj Quantum Information* **5**, 33 (2019).
- [45] Z. T. Wang, Y. Ashida, and M. Ueda, Deep reinforcement learning control of quantum cartpoles, *Phys. Rev. Lett.* **125**, 100401 (2020).
- [46] V. V. Sivak, A. Eickbusch, H. Liu, B. Royer, I. Tsoutsios, and M. H. Devoret, Model-free quantum control with reinforcement learning, *Phys. Rev. X* **12**, 011059 (2022).
- [47] F. Motzoi, J. M. Gambetta, P. Rebentrost, and F. K. Wilhelm, Simple pulses for elimination of leakage in weakly nonlinear qubits, *Phys. Rev. Lett.* **103**, 110501 (2009).
- [48] F. Yan, D. Campbell, P. Krantz, M. Kjaergaard, D. Kim, J. L. Yoder, D. Hover, A. Sears, A. J. Kerman, T. P. Orlando, *et al.*, Distinguishing coherent and thermal photon noise in a circuit quantum electrodynamical system, *Phys. Rev. Lett.* **120**, 260504 (2018).
- [49] S. Gustavsson, O. Zwier, J. Bylander, F. Yan, F. Yoshihara, Y. Nakamura, T. P. Orlando, and W. D. Oliver, Improving quantum gate fidelities by using a qubit to measure microwave pulse distortions, *Phys. Rev. Lett.* **110**, 040502 (2013).
- [50] V. V. Sivak, A. Eickbusch, B. Royer, S. Singh, I. Tsoutsios, S. Ganjam, A. Miano, B. L. Brock, A. Z. Ding, L. Frunzio, S. M. Girvin, R. J. Schoelkopf, and M. H. Devoret, Real-time quantum error correction beyond break-even, *Nature* **616**, 50 (2023).
- [51] V. Sivak, quantum-control-rl, <https://github.com/v-sivak/quantum-control-rl> (2022).
- [52] A. Di Paolo, T. E. Baker, A. Foley, D. Sénéchal, and A. Blais, Efficient modeling of superconducting quantum circuits with tensor networks, *npj Quantum Information* **7**, 11 (2021).
- [53] A. Mizel and Y. Yanay, Right-sizing fluxonium against charge noise, *Phys. Rev. B* **102**, 014512 (2020).
- [54] L. H. Pedersen, N. M. Møller, and K. Mølmer, Fidelity of quantum operations, *Phys. Lett. A* **367**, 47 (2007).